nature energy

Article

https://doi.org/10.1038/s41560-024-01615-6

Integrated rocksalt–polyanion cathodes with excess lithium and stabilized cycling

Received: 8 January 2024

Accepted: 24 July 2024

Published online: 23 August 2024

Check for updates

Yimeng Huang[1], Yanhao Dong[2,3] ✉, Yang Yang[4], Tongchao Liu[5], Moonsu Yoon[3,6], Sipei Li[3], Baoming Wang[3], Ethan Yupeng Zheng[1], Jinhyuk Lee[7], Yongwen Sun[4], Ying Han[4], Jim Ciston[8], Colin Ophus[8], Chengyu Song[8], Aubrey Penn[9], Yaqi Liao[10], Haijin Ji[10], Ting Shi[10], Mengyi Liao[10], Zexiao Cheng[10], Jingwei Xiang[10], Yu Peng[11], Lu Ma[12], Xianghui Xiao[12], Wang Hay Kan[13,14], Huaican Chen[13,14], Wen Yin[13,14], Lingling Guo[15], Wei-Ren Liu[16], Rasu Muruganantham[16], Chun-Chuen Yang[17], Yuntong Zhu[1], Qingjie Li[3] & Ju Li[1,3] ✉

Co- and Ni-free disordered rocksalt cathodes utilize oxygen redox to increase the energy density of lithium-ion batteries, but it is challenging to achieve good cycle life at high voltages >4.5 V (versus Li/Li$^+$). Here we report a family of Li-excess Mn-rich cathodes that integrates rocksalt- and polyanion-type structures. Following design rules for cation filling and ordering, we demonstrate the bulk incorporation of polyanion groups into the rocksalt lattice. This integration bridges the two primary families of lithium-ion battery cathodes—layered/spinel and phosphate oxides—dramatically enhancing the cycling stability of disordered rocksalt cathodes with 4.8 V upper cut-off voltage. The cathode exhibits high gravimetric energy densities above 1,100 Wh kg^{-1} and >70% retention over 100 cycles. This study opens up a broad compositional space for developing battery cathodes using earth-abundant elements such as Mn and Fe.

Rapid growth of electricity storage capabilities with lithium-ion batteries (LIBs) is required to realize a sustainable energy infrastructure[1]. In terms of resources, Co is ~5× the price of Li on a molar basis[2,3], and Ni is ~2× (ref. 3); thus, we would run into Co or Ni crises before Li. For advanced LIB cathodes, eliminating Co and Ni usage would greatly improve the scalability of electricity storage[4]. Disordered rocksalt (DRX) cathodes[5,6] are attractive for being potentially Co- and Ni-free, while having high energy densities (approaching 1,100 Wh kg^{-1} (ref. 7)). On the other hand, to reach high energy densities (>900 Wh kg^{-1}), high upper cut-off voltages (for example, 4.8 V versus Li/Li$^+$ for DRX[7–11]) are required for cathodes, which means highly delithiated states with most of the Li$^+$-hosting sites vacant. This often triggers the participation of oxygen anion redox and eventually irreversible oxygen loss, as delithiation lowers the Fermi level towards or dropping below the top of the oxygen 2*p* band, especially at the surface and interfaces[6,12–14]. A heavy usage of hybrid anion- and cation-redox with more exotic oxygen valence $O^{\alpha-}$ ($0 < \alpha < 2$) challenges the cycling stability of the cathode since $O^{\alpha-}$ tends to be more mobile, leading to percolating lattice oxygen diffusion to the reactive surface, extensive side reactions with the electrolyte and finally structural and chemical instability at the surface and in the bulk[15–19]. These are critical issues for DRX[6,20] and other high-energy-density cathodes[16,21].

LIB cathodes are mainly constructed on face-centred cubic (FCC) oxygen or lower-symmetry polyanion framework (hexagonal close-packed, HCP, oxygen for $LiFePO_4$, the most useful polyanion cathode). The former has cation ordering in the parent rocksalt structure, which includes high-energy-density cathodes of $LiCoO_2$, Ni-rich layered cathodes and Li-/Mn-rich layered cathodes[22,23] (spinel and DRX cathodes are also rocksalt structure derivatives with FCC oxygen sublattice). They have high theoretical capacities >270 mAh g^{-1}, and extensive research has been conducted to improve their high-voltage stability. The latter is exemplified by $LiFePO_4$, with exceptional structural, electrochemical and thermal stability, yet limited by the low theoretical capacity (170 mAh g^{-1}) and low energy density at the cathode level[24–26].

A full list of affiliations appears at the end of the paper. e-mail: dongyanhao@tsinghua.edu.cn; liju@mit.edu

https://doi.org/10.1038/s41560-024-01615-6

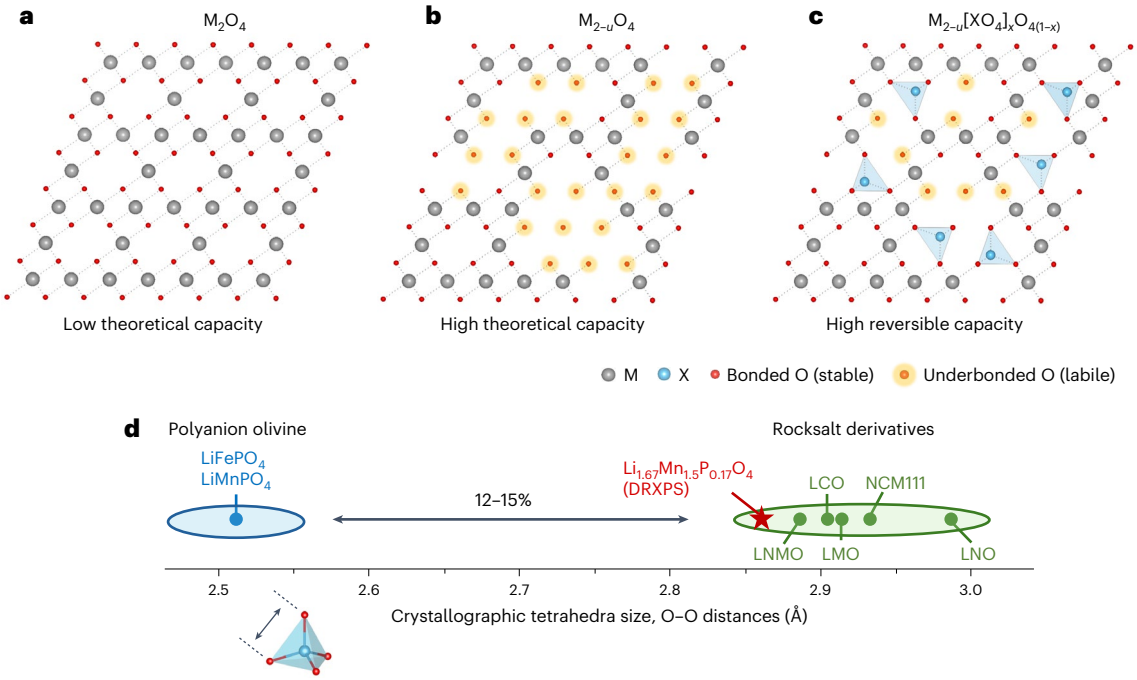

Fig. 1 | Design of DRXPS cathodes. a, The structure of M_2O_4. **b**, The structure of $M_{2-u}O_4$. **c**, The structure of $M_{2-u}[XO_4]_xO_{4(1-x)}$. **d**, Comparison of crystallographic tetrahedra size for polyanion olivine and rocksalt-type cathodes. LMO, $LiMn_2O_4$; LNMO, $LiNi_{0.5}Mn_{1.5}O_4$; LCO, $LiCoO_2$; NCM111, $LiNi_{1/3}Co_{1/3}Mn_{1/3}O_2$; LNO, $LiNiO_2$.

Marriage between the two families may offer synergistically improved energy density and stability. However, few reports[27] of their integration testify to the incompatibility between rocksalt and polyanion structures.

This work seeks to resolve the above conundrum with the invention of integrated rocksalt–polyanion cathodes. These compositions originate from DRX chemistries, and a major effort here is to improve the cycling stability under high upper cut-off voltages (required to deliver high capacity and energy density). We successfully produced a family of Li-excess Co- and Ni-free disordered rocksalt–polyanionic spinel (DRXPS) cathodes, with a general chemical formula of $Li_{2+u-v}M_{2-u}[XO_4]_xO_{4(1-x)}$. Here, *M* denotes transition metals such as Mn and Fe, XO_4 denotes polyanion groups such as PO_4, SiO_4 and SO_4, and *u*, *v* and *x* describe the designed stoichiometries. This family of compounds is called DRXPS because they are designed on a parent DRX structure and have bulk polyanion incorporation and spinel-type cation ordering (that gives a spinel diffraction pattern). Remarkable improvements of the cycling stability over reported DRX cathodes have been achieved in $Li_{1.67}Mn_{1.5}P_{0.17}O_4$, $Li_{1.67}Mn_{1.5}B_{0.17}O_4$, $Li_{1.67}Mn_{1.25}Fe_{0.25}P_{0.17}O_4$ and four more compositions, all belonging to the DRXPS family. The DRXPS cathodes have high capacities (>350 mAh g^{-1}), high energy densities (>1,100 Wh kg^{-1}), stable cycling (>70% energy density retention over 100 cycles), good rate performance and a highly tunable compositional space. The general design principles and experimental efforts presented here offer avenues for the future development of Co- and Ni-free cathodes.

Materials design

Our task is to design high-capacity oxide cathodes with excess Li, anion redox activity, bulk polyanion incorporation and good electrochemical stability. Starting from the high-capacity FCC oxygen framework, a three-dimensionally connected spinel structure M_2O_4 (Fig. 1a, Li is not shown for simplicity) provides the best hybridization between transition metal (M) *d* and oxygen 2*p* orbitals under the constrained Li/M molar ratio of 1 (each oxygen is coordinated with one tetrahedral Li and three octahedral M). Further raising the Li/M molar ratio above 1 (that is, replacing some M in Fig. 1a by Li) increases the theoretical capacity, and anion redox is simultaneously activated with underbonded oxygen (Fig. 1b). These underbonded oxygen can be oxidized upon charging to high voltages and may eventually leave the lattice in the form of outgassing if a percolative kinetic pathway exists from the bulk to the surface[28]. We aim to shut down the labile oxygen percolation by incorporating some polyanion groups into the Li-excess lattice (Fig. 1c), utilizing the strong X–O covalent bonds to mitigate oxygen instability.

Practical realization of the above is challenging and comes to the same incompatibility issue between rocksalt and polyanion structures discussed above. The main reasons are twofold. First, the cations in polyanion cathodes are not close-packed. The octahedral sites face-shared with XO_4 tetrahedra need to be empty[24]. This conflicts with cation-filling rules in layered and DRX cathodes (the octahedral sites are fully occupied). Second, X–O covalent bonds are short and strong, which results in much shorter O–O distances (characterizing the tetrahedral size) than the ones in rocksalt-structure cathodes. For example, the true tetrahedra size calculated from the P–O bond length in the polyanion olivine cathode $LiFePO_4$ (refs. 29,30) is 12–15% smaller than that in rocksalt-structure cathodes[31–34] (Fig. 1d). This would result in large lattice distortion and, thus, difficulty in making a solid-solution phase between XO_4 polyanions and 'normal O' anions.

We propose the following solution to the two problems mentioned above. For the first one, cation deficiency is an effective approach. Specifically, we were inspired by the polyhedral occupation rules in spinel cathodes: octahedra at 16d sites are fully occupied, and octahedra at 16c sites (face-shared with tetrahedra at 8a sites) are empty. So spinel-like cation ordering is preferred. For the second one, typical high-temperature solid-state synthesis would not work, and we resort to lower-temperature mechanochemical synthesis. Without going into the detailed derivations of the optimal values of stoichiometry (*u*, *v* and *x*) in Supplementary Note 1, we show in the following sections that the above simple design rules are powerful enough to guide the synthesis of the DRXPS cathode series.

Structure and morphology of prototype $Li_{1.67}Mn_{1.5}P_{0.17}O_4$

A prototype DRXPS cathode $Li_{1.67}Mn_{1.5}P_{0.17}O_4$ was synthesized by a one-pot mechanochemical method. The obtained sample has a

https://doi.org/10.1038/s41560-024-01615-6

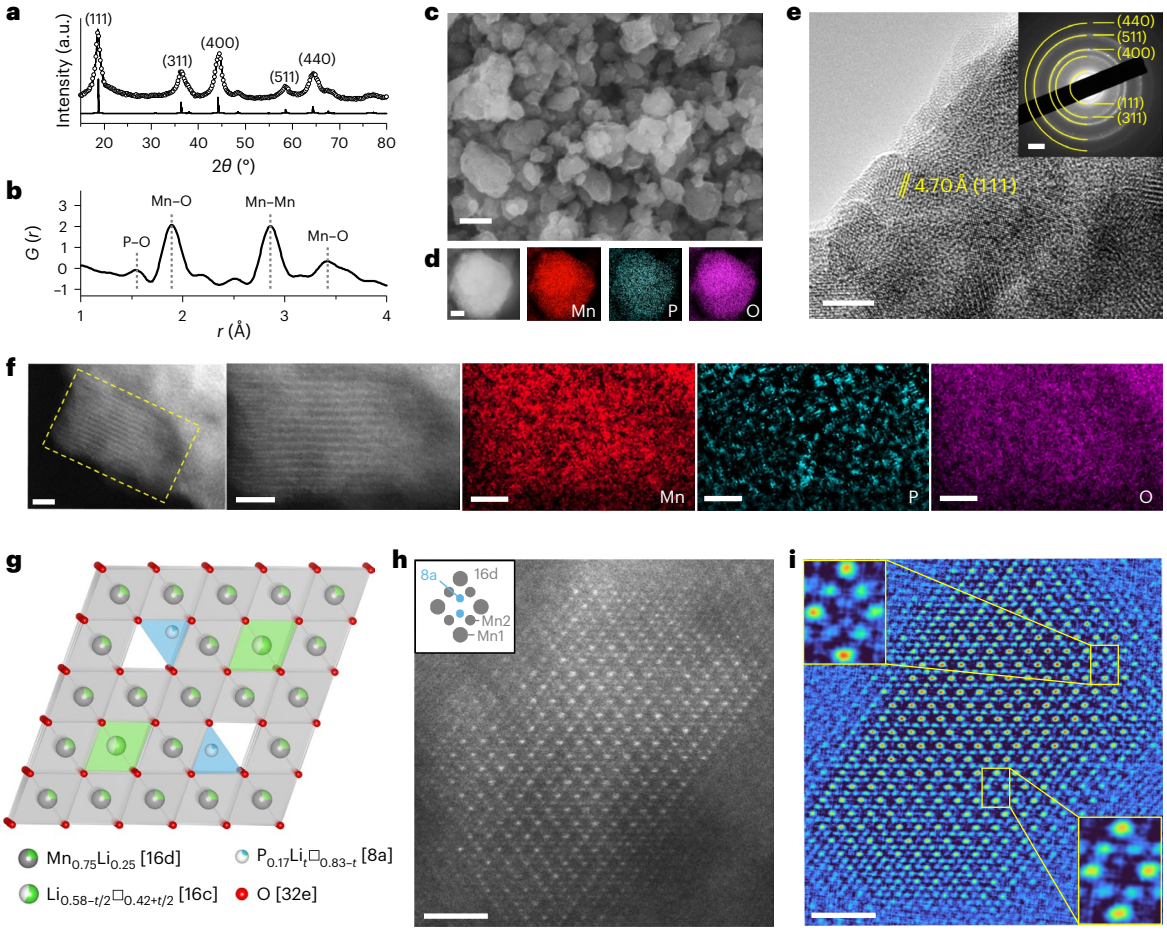

Fig. 2 | Structural characterization of $Li_{1.67}Mn_{1.5}P_{0.17}O_4$. **a**, XRD patterns of $Li_{1.67}Mn_{1.5}P_{0.17}O_4$. Open black circles are experimental, and solid black line is calculated. **b**, PDF of $Li_{1.67}Mn_{1.5}P_{0.17}O_4$. $G(r) = 4\pi r(\rho(r) - \rho_0)$, where $\rho(r)$ is the local atomic number density at distance r from a reference atom, and ρ_0 is the average atomic density of the material. **c**, SEM image of $Li_{1.67}Mn_{1.5}P_{0.17}O_4$. Scale bar, 200 nm. **d**, STEM–EDS mapping of $Li_{1.67}Mn_{1.5}P_{0.17}O_4$. Scale bar, 100 nm. **e**, TEM image of $Li_{1.67}Mn_{1.5}P_{0.17}O_4$. Scale bar, 5 nm. Inset: SAED pattern. Scale bar, 2 nm^{-1}. **f**, STEM–EELS mapping of Mn, P and O, performed on a single-crystal grain close to a zone axis, as indicated by the yellow dashed box. Note that the EELS signal of P is very weak due to the small atomic ratio of P in the composition; thus, the data supports but does not prove the uniform spatial distribution of P. Scale bars, 2 nm. **g**, Structural model of $Li_{1.67}Mn_{1.5}P_{0.17}O_4$. **h**, HAADF-STEM image of $Li_{1.67}Mn_{1.5}P_{0.17}O_4$. Inset: Atomic positions with alternating intensities at 16d sites, characteristic of a spinel structure. Scale bar, 1 nm. **i**, Filtered image of **h**. Insets: 16d and 8a site signals. Scale bar, 1 nm.

composition close to the designed stoichiometry (shown by the inductively coupled plasma mass spectrometry (ICP-MS) data in Supplementary Table 1). Its X-ray diffraction (XRD) pattern (Fig. 2a) matches with a single-phase cubic spinel structure ($a = b = c$, $\alpha = \beta = \gamma = 90°$; Supplementary Fig. 1). Rietveld refinement yields a lattice constant $a = 8.1527$ Å (Supplementary Fig. 1 and Supplementary Table 2), which is slightly smaller than those of spinel cathodes (8.246 Å for $LiMn_2O_4$ and 8.172 Å for $LiNi_{0.5}Mn_{1.5}O_4$). Neutron powder diffraction measurement (Supplementary Fig. 2) and refinement (Supplementary Table 3) were further conducted on $Li_{1.67}Mn_{1.5}P_{0.17}O_4$ for better sensitivity on Li sites, which shows consistent results with XRD measurements. For more structural information, we conducted pair distribution function (PDF) analysis on $Li_{1.67}Mn_{1.5}P_{0.17}O_4$ (Fig. 2b) and compared with references of $LiMn_2O_4$ and $LiFePO_4$ (Supplementary Fig. 3). First-nearest-neighbour P–O pair at 1.549 Å was observed, which is slightly longer than the P–O pair in the PO_4 group of $LiFePO_4$ (1.520 Å). First-nearest-neighbour Mn–O pair at 1.893 Å and Mn–Mn pair 2.858 Å were observed, which are slightly shorter than the corresponding ones in $LiMn_2O_4$ (1.903 Å for Mn–O and 2.887 Å for Mn–Mn). These elastic straining effects are consistent with our materials design (tensile strained for XO_4 compared with $LiFePO_4$ and compressive strained for MO_6 compared with $LiMn_2O_4$). The effect smears at longer distances, for example, second-nearest-neighbour Mn–O distances (3.418 Å) are similar in $Li_{1.67}Mn_{1.5}P_{0.17}O_4$ and $LiMn_2O_4$. Raman spectroscopy measurement (Supplementary Fig. 4) was conducted for local structure analysis. The Raman peak at ~940 cm^{-1} can be assigned to the A_{1g} mode of PO_4 (ref. 35), the peak at ~600 cm^{-1} can be assigned to the symmetric stretching mode of MnO_6 (refs. 36,37) and the peaks at 420–490 cm^{-1} can be assigned to the symmetric stretching modes of LiO_4 and LiO_6 (ref. 36). These Raman features support tetrahedral occupation of P, octahedral occupation of Mn and mixed tetrahedral/octahedral occupations of Li.

The scanning electron microscopy (SEM) image in Fig. 2c shows that $Li_{1.67}Mn_{1.5}P_{0.17}O_4$ has an average size of ~150 nm for the agglomerates (see size distribution in Supplementary Fig. 5). Energy dispersive spectroscopy mapping in scanning transmission electron microscopy (STEM-EDS) (Fig. 2d) shows a uniform distribution of Mn, P and O. The transmission electron microscopy (TEM) image in Fig. 2e shows that the particles in Fig. 2c are polycrystalline, consisting of 5–10 nm 'primary' particles that are crystalline. A characteristic lattice spacing $d = 4.70$ Å can be identified, corresponding to the (111) plane of the spinel structure. The selected area electron diffraction (SAED) pattern (Fig. 2e, inset) further confirms the polycrystallinity, with diffraction rings corresponding to the (111), (311), (400), (511) and (440) peaks. Figure 2f shows the electron energy loss spectroscopy (EELS) mapping

https://doi.org/10.1038/s41560-024-01615-6

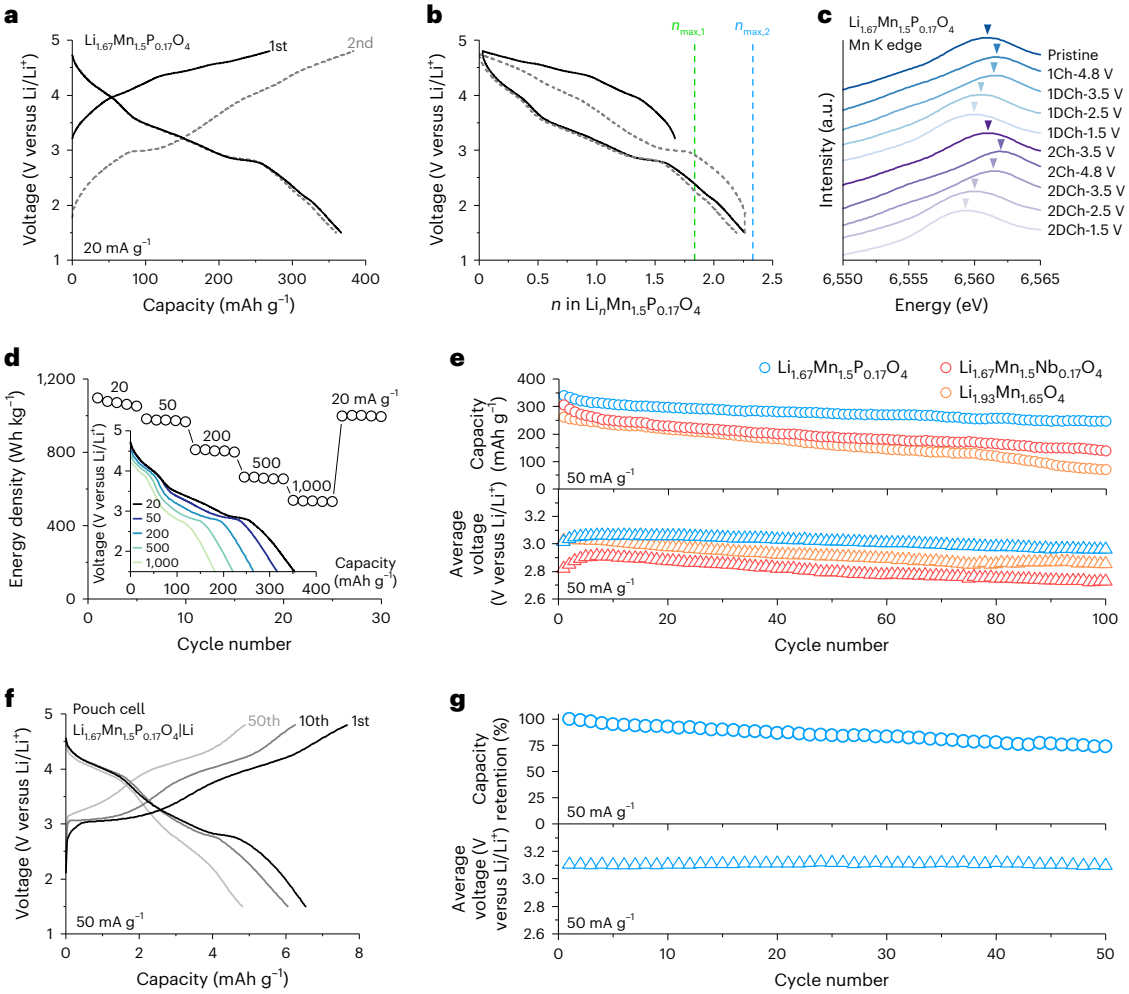

Fig. 3 | Electrochemistry and redox mechanism of $Li_{1.67}Mn_{1.5}P_{0.17}O_4$. **a**, Voltage profiles of $Li_{1.67}Mn_{1.5}P_{0.17}O_4$ in the initial two formation cycles between 1.5 and 4.8 V versus Li/Li^+ at 20 mA g^{-1}. **b**, Capacity from **a** converted to Li content *n*. The theoretical capacity is marked by the dashed lines under two assumptions: if Li tetrahedral occupation is not allowed (dashed green line); if Li tetrahedral occupation is allowed (dashed blue line). **c**, Mn K-edge XANES spectra of $Li_{1.67}Mn_{1.5}P_{0.17}O_4$ in the first two cycles. **d**, Rate performance test of $Li_{1.67}Mn_{1.5}P_{0.17}O_4$ at 20, 50, 200, 500 and 1,000 mA g^{-1} (the same cell was used). Inset: Voltage profiles of the first discharge cycle at 20, 50, 200, 500 and 1,000 mA g^{-1}. **e**, Discharge capacity (top) and average discharge voltage (bottom) retention of $Li_{1.67}Mn_{1.5}P_{0.17}O_4$, $Li_{1.67}Mn_{1.5}Nb_{0.17}O_4$ and $Li_{1.93}Mn_{1.65}O_4$ in 100 cycles between 1.5 and 4.8 V versus Li/Li^+ at 50 mA g^{-1}, following the two initial formation cycles at 20 mA g^{-1} (not shown). **f**, Voltage profiles of ($Li_{1.67}Mn_{1.5}P_{0.17}O_4$|Li) pouch cell at the 1st, 10th and 50th cycle between 1.5 and 4.8 V versus Li/Li^+ at 50 mA g^{-1} (following two formation cycles at 20 mA g^{-1}). **g**, Discharge capacity (top) and average discharge voltage (bottom) retention of the pouch cell during 50 mA g^{-1} cycling.

of a $Li_{1.67}Mn_{1.5}P_{0.17}O_4$ primary particle, with uniform Mn, P and O distributions that support the bulk incorporation of P in the lattice (additional evidence from STEM-EDS is shown in Supplementary Fig. 6).

With the above information, we constructed the structural model (Fig. 2g). Per chemical formula $Li_{1.67}Mn_{1.5}P_{0.17}O_4$, 4 O at 32e sites form the FCC anion framework, 1.5 Mn occupy 3/4 of the 16d cation octahedral sites and 0.17 P occupy 1/6 of the 8a cation tetrahedral sites. As 16d sites should be fully occupied in spinel structure, the remaining 1/4 should be occupied by 0.5 Li. This leaves 1.17 Li that occupy either 8a or 16c sites. Therefore, using '□' to denote cation vacancy (that is, unoccupied tetrahedral/octahedral sites), we can express the structural model as $(P_{0.17}Li_t\square_{0.83-t})_{8a}(Li_{1.17-t}\square_{0.83+t})_{16c}(Li_{0.5}Mn_{1.5})_{16d}(O_4)_{32e}$. The calculated XRD pattern from the constructed structure (Fig. 2a, solid black curve) matches well with the experimental one, and it is close to the refined structure (Supplementary Table 2). The proposed structural model is further supported by high-angle annular dark-field scanning transmission electron microscopy (HAADF-STEM) image in Fig. 2h. Spinel-type cation ordering with Mn atoms at 16d octahedral sites, viewed along the [110] zone axis, is clearly shown. The alternating intensities at 16d sites (brighter at Mn1 sites and darker at Mn2 sites; schematics shown in the inset of Fig. 2h) are also a characteristic feature of the spinel structure[38,39]. Further analysis using a least absolute shrinkage and selection operator (LASSO) filter (Methods) was applied to obtain Fig. 2i. In addition to 16d site signals, some intensities are present at 8a sites (see top-left and bottom-right insets of Fig. 2i). These 8a site signals are possibly attributed to P, as Li has almost no contrast under the HAADF mode and it is difficult for Mn to enter tetrahedral sites.

Electrochemistry and redox mechanism of $Li_{1.67}Mn_{1.5}P_{0.17}O_4$

We first evaluated the electrochemical performance of $Li_{1.67}Mn_{1.5}P_{0.17}O_4$ in coin-type half cells between 1.5 and 4.8 V versus Li/Li^+ at room temperature. Figure 3a shows the galvanostatic charge–discharge curves of the first two cycles at 20 mA g^{-1}, with high discharge capacities of ~365 mAh g^{-1} and high discharge energy densities of ~1,120 Wh kg^{-1}. Converting the capacity to stoichiometry, we estimated a high Li usage of 1.63 Li removal (out of 1.67 Li) per formula unit (Fig. 3b) in the first charge. Since Mn in $Li_{1.67}Mn_{1.5}P_{0.17}O_4$ has an average valence of +3.67 (a slightly lower Mn average valence may be possible depending on synthesis conditions) and Mn^{3+}/Mn^{4+} can only charge-compensate

https://doi.org/10.1038/s41560-024-01615-6

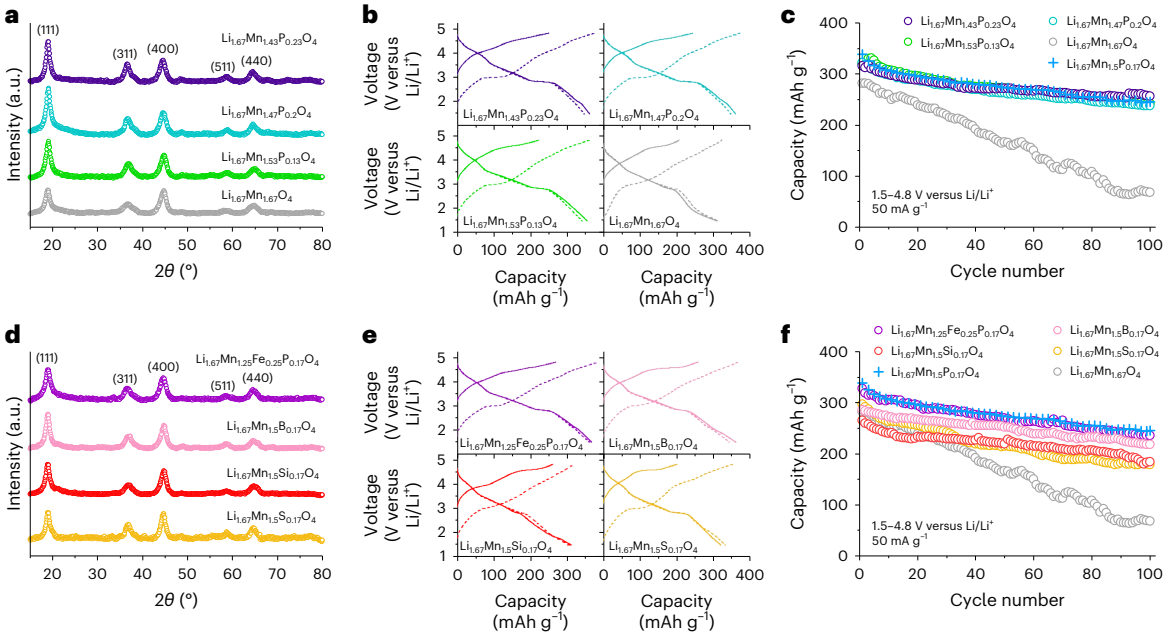

Fig. 4 | Structure and performance of diverse compositions of DRXPS. **a**, XRD patterns of $Li_{1.67}Mn_{1.67-x}P_xO_4$ ($x = 0, 0.13, 0.2, 0.23$). **b**, Voltage profiles of the initial two formation cycles of $Li_{1.67}Mn_{1.67-x}P_xO_4$ ($x = 0$, 0.13, 0.2 and 0.23) between 1.5 and 4.8 V versus Li/Li^+ at 20 mA g^{-1}. **c**, Discharge capacity retention of $Li_{1.67}Mn_{1.67-x}P_xO_4$ ($x = 0$, 0.13, 0.17, 0.2 and 0.23) in the first 100 cycles, between 1.5 and 4.8 V versus Li/Li^+ at 50 mA g^{-1}, after two formation cycles at 20 mA g^{-1} (not shown). **d**, XRD patterns of $Li_{1.67}Mn_{1.25}Fe_{0.25}P_{0.17}O_4$ and $Li_{1.67}Mn_{1.5}X_{0.17}O_4$ (X = B, Si, S). **e**, Voltage profiles of the initial two formation cycles of $Li_{1.67}Mn_{1.25}Fe_{0.25}P_{0.17}O_4$ and $Li_{1.67}Mn_{1.5}X_{0.17}O_4$ (X = B, Si, S) between 1.5 and 4.8 V versus Li/Li^+ at 20 mA g^{-1}. **f**, Discharge capacity retention of $Li_{1.67}Mn_{1.25}Fe_{0.25}P_{0.17}O_4$ and $Li_{1.67}Mn_{1.5}X_{0.17}O_4$ (X = B, Si, S) in the first 100 cycles, between 1.5 and 4.8 V versus Li/Li^+ at 50 mA g^{-1}, after two formation cycles at 20 mA g^{-1} (not shown). Data for $Li_{1.67}Mn_{1.5}P_{0.17}O_4$ and $Li_{1.67}Mn_{1.67}O_4$ are also shown for reference.

for 0.5 Li removal, we expect active participation of anion redox $O^{2-}/O^{\alpha-}$ ($0 < \alpha < 2$). During the first discharge, 2.23 Li was inserted into the structure, ending with an over-lithiated composition of $Li_{2.27}Mn_{1.5}P_{0.17}O_4$. The over-lithiation should be charge-compensated by Mn reduction. The second cycle shows a similar discharge curve to the first one, indicating good reversibility.

To better understand the redox mechanism, we performed ex situ hard X-ray absorption spectroscopy. Figure 3c shows the Mn K-edge X-ray absorption near-edge structure (XANES) for $Li_{1.67}Mn_{1.5}P_{0.17}O_4$ at different states of charge (marked on the voltage profiles in Supplementary Fig. 7b). Since the near-edge structure depends on both the oxidation state and the bonding environment[40], we analysed Mn valence by comparing with reference spectra (Supplementary Fig. 7a). For the first two cycles, all Mn K-edge spectra stay higher in energy than the Mn_2O_3 (Mn^{3+}) reference and shift to higher energy (Mn oxidation) during charge and to lower energy (Mn reduction) during discharge, indicating active participation of reversible $Mn^{3+/4+}$ redox couple. For charge in the first (pristine to 1Ch-4.8V) and second cycle (1DCh-1.5V to 2Ch-4.8V), capacities of 269 and 384 mAh g^{-1} are observed (corresponding to Mn valence changes of +1.09 and +1.56), respectively. Meanwhile, Mn K edges for both charge half-cycles shift from between the Mn_2O_3 (Mn^{3+}) and MnO_2 (Mn^{4+}) reference spectra to close to MnO_2 (Mn^{4+}). This one-electron TM redox cannot account for the high reversible capacity by itself. For discharge to 3.5 V versus Li/Li^+ (1Ch-4.8V to 1DCh-3.5V and 2Ch-4.8V to 2DCh-3.5V), a capacity of ~96 mAh g^{-1} (corresponding to a Mn valence change of −0.39) are observed for both cycles, while the Mn K edges for both only experience minor downshifts. Therefore, active oxygen redox should also be involved during charge to 4.8 V versus Li/Li^+ and discharge to 3.5 V versus Li/Li^+ for the initial two cycles. Capacities below 3.5 V versus Li/Li^+ should be solely contributed by the $Mn^{3+/4+}$ redox couple since the Mn K edges lie between the Mn_2O_3 (Mn^{3+}) and MnO_2 (Mn^{4+}) spectra, and the shifts roughly match the expected Mn valence change (converted from the observed capacity). Towards the end of discharge, the average Mn valence stayed above +3, as shown by the extra ex situ measurements on the Mn K edge performed in the low voltage region (<2.5 V versus Li/Li^+) (Supplementary Fig. 8). This means that the population of Mn^{2+}, prone to dissolution in the electrolyte, is low in the cathode.

The rate performance of $Li_{1.67}Mn_{1.5}P_{0.17}O_4$ was tested from 20 mA g^{-1} to 1,000 mA g^{-1} (~5.5 C calculated from the charging time). Capacity retentions of 75% and 51% were observed when the galvanostatic current density increased from 20 mA g^{-1} to 200 mA g^{-1} and 1,000 mA g^{-1}, respectively (Fig. 3d and Supplementary Fig. 9). Galvanostatic intermittent titration technique (GITT) measurement was performed in the first discharge cycle for $Li_{1.67}Mn_{1.5}P_{0.17}O_4$ and polyanion-free reference sample $Li_{1.93}Mn_{1.65}O_4$ (Supplementary Fig. 10a). The former shows an average non-Ohmic loss of only 90 mV per titration step (Supplementary Fig. 10b). The calculated Li diffusivities are in the range of ~10^{-14} to 10^{-13} cm^2 s^{-1} (Supplementary Fig. 10c), which are higher than the commonly reported values (10^{-16} to 10^{-15} cm^2 s^{-1}) for DRX cathodes[20]. This shows facile Li^+ diffusion kinetics for the cation-deficient spinel structure of DRXPS. Comparing the non-Ohmic losses with $Li_{1.93}Mn_{1.65}O_4$ (Supplementary Fig. 10b), we found that the addition of polyanions in DRXPS does not harm Li^+ diffusion kinetics. The cycling performance of $Li_{1.67}Mn_{1.5}P_{0.17}O_4$ was tested at 50 mA g^{-1} between 1.5 and 4.8 V versus Li/Li^+, after two formation cycles at 20 mA g^{-1}. After 100 cycles, it has a capacity retention of 72% (Fig. 3e, top), an average discharge voltage maintained at >3 V versus Li/Li^+ (minimal voltage decay of <0.74 mV per cycle; Fig. 3e, bottom) and a discharge energy retention of 71% (Supplementary Fig. 11). For comparison, we tested the cycling performance of the similarly synthesized polyanion-free $Li_{1.67}Mn_{1.5}Nb_{0.17}O_4$ and $Li_{1.93}Mn_{1.65}O_4$ as control groups (Supplementary Fig. 12; both have spinel-like structures, and an average Mn valence of +3.67, similar to $Li_{1.67}Mn_{1.5}P_{0.17}O_4$). $Li_{1.67}Mn_{1.5}Nb_{0.17}O_4$/$Li_{1.93}Mn_{1.65}O_4$ show faster degradations with 45%/27% capacity retention (Fig. 3e, top) and 44%/25% energy density retention (Supplementary Fig. 11) after 100 cycles under the same testing conditions. dQ/dV analysis for $Li_{1.67}Mn_{1.5}P_{0.17}O_4$ and $Li_{1.93}Mn_{1.65}O_4$ (Supplementary Fig. 13) provides better visualization

of the improved oxygen redox reversibility at high voltages (>4.2 V versus Li/Li$^+$) for $Li_{1.67}Mn_{1.5}P_{0.17}O_4$. Remarkably, $Li_{1.67}Mn_{1.5}P_{0.17}O_4$ have suppressed gas evolution (in situ differential electrochemical mass spectrometry, DEMS, in Supplementary Fig. 14), Mn dissolution in the electrolyte (Supplementary Fig. 15a) and Mn deposition on the anode (Supplementary Fig. 15b) compared with $Li_{1.67}Mn_{1.5}Nb_{0.17}O_4$, all indicating stability enhancement in the former composition (more detailed comparisons between $Li_{1.67}Mn_{1.5}P_{0.17}O_4$ and $Li_{1.67}Mn_{1.5}Nb_{0.17}O_4$ are provided in Supplementary Note 2). The high-voltage cycling stability of $Li_{1.67}Mn_{1.5}P_{0.17}O_4$ is also superior over the DRX cathodes reported in the literature (see comparison in Supplementary Table 4 and Supplementary Fig. 16). Lastly, to evaluate the electrochemical performance of $Li_{1.67}Mn_{1.5}P_{0.17}O_4$ under more practically relevant conditions, we assembled $Li_{1.67}Mn_{1.5}P_{0.17}O_4$|Li metal anode pouch cells. A good capacity retention of 74% and stable discharge voltage around 3.11 V (Fig. 3f,g, with no voltage decay) have been achieved over 50 cycles at 50 mA g^{-1} between 1.5 and 4.8 V versus Li/Li$^+$. In addition, we fabricated thicker electrodes with higher active material weight ratio and achieved good cycling stability when the active material mass loading is increased to 5–10 mg cm^{-2} (Supplementary Fig. 17).

Exploring compositional space of DRXPS

The DRXPS family has a rich chemistry. To demonstrate, we show the following examples within the general formula $Li_{2+u-v}M_{2-u}[XO_4]_xO_{4(1-x)}$. We first varied the P content in $Li_{1.67}Mn_{1.67-x}P_xO_4$ ($0 \le x \le 0.5$). The XRD patterns of the four synthesized compounds are shown in Fig. 4a (more examples in Supplementary Fig. 18a). Phase-pure spinel structure readily forms at $x \le 0.27$, while the impurity phase begins to form at $x \ge 0.33$ (from unreacted MnO_2 precursor). To evaluate the electrochemical performance, we cycled $Li_{1.67}Mn_{1.67-x}P_xO_4$ at 50 mA g^{-1} between 1.5 and 4.8 V versus Li/Li$^+$, after two formation cycles at 20 mA g^{-1}. Figure 4b shows the voltage profiles of the four selected compositions in the initial two formation cycles. As shown in Fig. 4c and Supplementary Fig. 18b, PO_4 incorporation drastically improves the cycling stability over the P-free $Li_{1.67}Mn_{1.67}O_4$. For better quantifications, we compared the discharge energy density at the 25th cycle at 50 mA g^{-1} (Supplementary Fig. 18c) and benchmarked against 730 Wh kg^{-1} reported by Ji et al.[7] for DRX and related cathodes. We found that the relation between x and cycling performance resembles that of a volcano plot (also true at the 100th cycle; Supplementary Fig. 18d), and $0.13 \le x \le 0.23$ offers stabilized energy density of 867–890 Wh kg^{-1} at the 25th cycle. The experimentally observed volcano plot behaviour and x range are quantitatively consistent with analytical derivations ($0.159 \le x \le 0.222$ in Supplementary Note 1) based on our stated design principles. A detailed study of the compositions with varying u and v is provided in Supplementary Note 3.

We next practiced Mn–Fe substitution. Fe is another redox-active and earth-abundant element that attracts continuous interest. $Li_{1.67}Mn_{1.25}Fe_{0.25}P_{0.17}O_4$ was synthesized mechanochemically. The XRD pattern shows a single-phase cubic spinel structure (Fig. 4d; $a = b = c = 8.129$ Å, $\alpha = \beta = \gamma = 90°$). Under SEM, we confirmed that $Li_{1.67}Mn_{1.25}Fe_{0.25}P_{0.17}O_4$ consisted of polycrystalline particles (~200 nm; Supplementary Fig. 19a) with uniform elemental distributions (EDS mapping in Supplementary Fig. 19b) and fine primary nano particles (TEM in Supplementary Fig. 19c; a characteristic lattice spacing of 4.69 Å, corresponding to the (111) peak of the spinel structure, and SAED in the inset of Supplementary Fig. 19c showing polycrystalline diffraction rings that also match the phase). The electrochemical performance of $Li_{1.67}Mn_{1.25}Fe_{0.25}P_{0.17}O_4$ was tested between 1.5 and 4.8 V versus Li/Li$^+$ at room temperature. In the first cycle at 20 mA g^{-1} (Fig. 4e), it shows a discharge capacity of 327 mAh g^{-1} and a discharge energy density of 978 Wh kg^{-1}, which are slightly lower than the corresponding values for $Li_{1.67}Mn_{1.5}P_{0.17}O_4$. $Li_{1.67}Mn_{1.25}Fe_{0.25}P_{0.17}O_4$ shows exceptional cycling performance, with 72% capacity retention (Fig. 4f) and 67% energy density retention (Supplementary Fig. 20b) over 100 cycles at 50 mA g^{-1}. The substitution was extended to a higher Fe ratio to produce $Li_{1.67}MnFe_{0.5}P_{0.17}O_4$ and with some Ni to produce $Li_{1.67}Mn_{1.33}Ni_{0.17}P_{0.17}O_4$. The spinel phase has been identified for all these compositions (Supplementary Fig. 20a). Their cycling performances are compared with $Li_{1.67}Mn_{1.5}P_{0.17}O_4$ and $Li_{1.67}Mn_{1.25}Fe_{0.25}P_{0.17}O_4$ in Supplementary Fig. 20b. Discharge energy densities of 610–825 Wh kg^{-1} were obtained at the 25th cycle (Supplementary Fig. 20c), which demonstrates highly tunable transition metal chemistries in DRXPS.

We lastly studied different polyanion groups. In addition to the valence +5 P, we synthesized $Li_{1.67}Mn_{1.5}X_{0.17}O_4$ with X = +3 B, +4 Si and +6 S. These non-metallic elements all form strong covalent bonds with oxygen and can adopt a tetrahedral occupancy (that is, forming XO_4 groups). As shown by the XRD patterns in Fig. 4d, phase-pure spinel structures have been identified for $Li_{1.67}Mn_{1.5}B_{0.17}O_4$ and $Li_{1.67}Mn_{1.5}Si_{0.17}O_4$, while minor impurity peaks matching MnO_2 (precursor) exists in $Li_{1.67}Mn_{1.5}S_{0.17}O_4$ in addition to the main spinel phase. Microscopy characterizations in Supplementary Fig. 19d–f of a selected composition, $Li_{1.67}Mn_{1.5}B_{0.17}O_4$, show a polycrystalline particle morphology with ultrafine primary ones that are well crystalized. The electrochemical performance of $Li_{1.67}Mn_{1.5}X_{0.17}O_4$ was tested between 1.5 and 4.8 V versus Li/Li$^+$ at room temperature. Figure 4e shows the galvanostatic charge–discharge curves of the first two cycles at 20 mA g^{-1} for $Li_{1.67}Mn_{1.5}B_{0.17}O_4$, $Li_{1.67}Mn_{1.5}Si_{0.17}O_4$ and $Li_{1.67}Mn_{1.5}S_{0.17}O_4$. Among the three compositions, $Li_{1.67}Mn_{1.5}B_{0.17}O_4$ has the highest discharge capacity of ~360 mAh g^{-1} and the highest discharge energy density of ~1,070 Wh kg^{-1}, which are comparable with the corresponding values of $Li_{1.67}Mn_{1.5}P_{0.17}O_4$. When cycled at a higher rate of 50 mA g^{-1}, good cycling stability can be identified and the discharge capacity (Fig. 4f) and energy density (Supplementary Fig. 21) at the 25th cycle (after two formation cycles) follows the rank of $Li_{1.67}Mn_{1.5}P_{0.17}O_4$ > $Li_{1.67}Mn_{1.5}B_{0.17}O_4$ > $Li_{1.67}Mn_{1.5}S_{0.17}O_4$ > $Li_{1.67}Mn_{1.5}Si_{0.17}O_4$. Remarkably, all these compositions show great improvements over the polyanion-free compositions (for example, $Li_{1.67}Mn_{1.5}Nb_{0.17}O_4$ and $Li_{1.93}Mn_{1.65}O_4$). Therefore, we conclude that the integrated rocksalt–polyanion structure presented in this Article is a general methodology to improve the stability of high-energy-density oxide cathodes, especially DRX cathodes.

Conclusions

We demonstrated a promising family of Co- and Ni-free DRXPS cathodes with stabilized high hybrid anion- and cation-redox capacities and energy densities. It overcomes the key bottleneck of poor high-voltage cyclability for the development of DRX cathodes and their derivatives. Despite the encouraging results, there remain issues to be addressed to enable the practical use of DRXPS cathodes. First, the ratio of the active materials in the composite cathode needs to be increased to >90 wt%, while the ratio of the conductive carbon needs to be substantially lowered for better practicality (for example, increase volumetric energy density, calculated in Supplementary Table 5). This can be resolved with a thin layer of uniform carbon coating, as is the case for $LiFePO_4$, which can improve the long-range electron percolation in the composite electrode. Second, the cycling stability needs to be further improved to allow for >500–1,000 deep charge–discharge cycles. This can be resolved by applying coatings, minor lattice doping, concentration-gradient design, and advanced electrolytes and electrolyte additives. With the above issues addressed, scalable synthesis methods (Supplementary Note 4) should be developed, and DRXPS cathodes should be evaluated in practical full cells (supported by pre-lithiation technologies for the first-cycle overlithiation). We look forward to rapid progress in developing Co- and Ni-free DRXPS cathodes, and their practical applications in sustainable energy.

Methods

Synthesis

All compositions were synthesized using a one-pot room-temperature mechanochemical synthesis method. Li_2O, Mn_2O_3, MnO_2, Li_3PO_4, Fe_2O_3, B_2O_3, Li_2SO_4 and SiO_2 (all from Sigma-Aldrich, 99% purity) precursors were directly mixed using the Fritsch Pulverisette 7 Premium Line planetary

ball mill, according to stoichiometry (for example, $Li_{1.67}Mn_{1.5}P_{0.17}O_4$ = 0.58 Li_2O + 0.25 Mn_2O_3 + MnO_2 + 0.17 Li_3PO_4). Precursor powders with a total weight of around 5 g were put into an 80 ml stainless-steel jar, with 25 10-mm-diameter stainless steel balls (the powder-to-ball weight ratio of was 1:20) and mixed in air at room temperature under 800 rpm for 5 h. No additional heat treatment was involved.

Materials characterizations

ICP-MS was conducted on Agilent 730. Inductively coupled plasma optical emission spectroscopy (ICP-OES) was conducted on Agilent 5100 VDV. High resolution X-ray diffraction data were collected at Beamline 11-BM, Argonne National Laboratory, in the 2θ range of 0.5–50° with a step size of 0.001°, counting time of 0.1 s per step, and a wavelength of λ = 0.458961 Å at 295 K and λ = 0.458956 Å at 100 K. Fine-ground polycrystalline powders were loaded into a ϕ0.8 mm Kapton capillary for installation on a magnetic sample base used by the beamline sample changer. The sample was spun continuously at 5,600 rpm during data collection. X-ray PDF measurements were completed at room temperature at the 11-ID beamline at the Advanced Photon Source, Argonne National Laboratory, using a General Electric amorphous Si two-dimensional detector. The sample to detect or distance was fixed at 117.13 mm, and synchrotron X-rays with the wavelength of 0.2127 Å were utilized with a 0.2 mm × 0.2 mm beam size. All other XRD measurements were conducted on an Aeris Research Edition X-ray diffractometer using a Cu target under 40 kV and 15 mA, in the 2θ range of 15–80°. Time-of-flight neutron diffraction was conducted at Multi Physics Instrument in China Spallation Neutron Source, operating at 160 kW beam power with 25 Hz repetition rate. About 3 g of powder was put into V can, and the measurement time was about 3 h. The diffraction dataset was analysed using GSAS II. Raman spectroscopy was conducted on WITec alpha300 R Raman microscope. Laser wavelength of 532 nm was applied with a power of 5 mW, a grating of 300 g mm^{-1} and a spectral resolution of 0.1 cm^{-1} to acquire the Raman data. Each spectrum was collected with five scans and 10 s integration for each scan. SEM was conducted on a Zeiss Merlin high-resolution scanning electron microscope. TEM, SAED and EDS were conducted on a JEOL 2010F transmission electron microscope with an acceleration voltage of 200 kV. Ex situ XANES measurement was conducted at the 7-BM beamline at the National Synchrotron Light Source II, Brookhaven National Laboratory, and at the BL17B1 beamline of the Shanghai Synchrotron Radiation Facility (SSRF), at a typical energy of the storage ring of 3.5 GeV under the 'top-up' mode with a constant current of 210 mA. HAADF-STEM and EELS mapping were performed using the TEAM I transmission electron microscope at the National Center for Electron Microscopy, Lawrence Berkeley National Laboratory. This microscope is double aberration-corrected and operates at 300 keV, with a convergence angle of 30 mrad and a beam current of 70 pA. A LASSO filter with thickness effect removal and a turbo colormap were applied to the HAADF-STEM image for better visualization of site occupations. The EELS mapping was acquired using a Gatan GIF Continuum K3 System. During the EELS measurement, the aperture size is 5 mm, yielding an EELS collection semi angle of 150 mrad, the dispersion is 0.18 eV Ch^{-1} and the step size is 0.0996 nm. The grain selected for EELS measurement is close to a zone axis such that some lattice fringes can be seen. HAADF-STEM with EDS was performed using Thermo Fisher Scientific Themis Z G3 aberration-corrected scanning transmission electron microscope at MIT.Nano, operated at 200 kV with a beam current of 30–40 pA and 19 mrad convergence angle. EDS was collected with a 100 pA beam current on Super-X EDS detectors. X-ray fluorescence (XRF) was performed on a Bruker Tracer-III SD Portable XRF.

Electrochemical measurements

All electrodes for electrochemical testing were prepared by mixing 70 wt% active material, 20 wt% conductive carbon (Timcal Super C65) and 10 wt% polyvinylidene fluoride (Sigma-Aldrich) using *N*-methyl-2-pyrrolidone (Sigma-Aldrich) as the solvent to form a slurry, which was then casted onto an aluminium foil using a 250-µm-gap doctor blade. The loading of the electrode films was 2–3 mg cm^{-1}. A polypropylene (Celgard 2400) membrane was used as the separator, and 1.2 M $LiPF_6$ dissolved in ethylene carbonate:ethyl methyl carbonate = 30:70 wt% solution (Gotion) was used as the electrolyte. Li metal foil was used as the counter and reference electrode. Coin-type cells (CR2032) were assembled in an argon-filled glove box (MBraun). Electrochemical testing of the coin cells was conducted on a Landt CT2001A battery tester (Wuhan Lanhe Electronics) and a Neware battery tester (BTS-9000) at room temperature. Galvanostatic cycling was performed between 1.5 and 4.8 V versus Li/Li^+ at 20 mA g^{-1} for the initial two formation cycles, and then at 50 mA g^{-1} onwards. The rate performance test was performed between 1.5 and 4.8 V versus Li/Li^+ at 20, 50, 200, 500 and 1,000 mA g^{-1} for five cycles each, on the same coin cell for each composition. GITT measurements were performed between 1.5 and 4.8 V versus Li/Li^+, with 20 mA g^{-1} current pulse for 20 min, followed by a 2 h relaxation step. For pouch cells, cathode film with active material loading of 2.5 mg cm^{-1} and dimension of 3 cm × 4 cm was used, paired with Li metal foil. The electrolyte, separator and galvanostatic cycling test conditions were the same as coin cells. For XANES measurement, electrode samples were prepared by disassembling coin cells that were charged/discharged to a specific voltage, and then rinsed with dimethyl ether for 2 min. For ICP-OES measurement, electrolyte samples were prepared by disassembling coin cells after a certain number of cycles and charged to 4.8 V versus Li/Li^+, and then soaking the cycled cathode film in fresh electrolyte for 10 days at room temperature. For ex situ and XRF measurements, cathode and anode films (lithium metal disc) were obtained by disassembling coin cells after a certain number of cycles and discharged to 3 V versus Li/Li^+, and then rinsed with dimethyl ether for 2 min. In situ DEMS experiments were carried out using a commercial mass spectrometer (Linglu Instruments, Shanghai). The DEMS cell was assembled with a Swagelok-type cell, where the diameter and mass loading of the electrode disc were 16 mm and 10 mg cm^{-2}, respectively. The assembled cell was connected to the gas path of the mass spectrometer (Pfeiffer, OminiStar GSD 320). The total carrier gas (Ar) was 3 ml min^{-1}, and the flow was 3 ml min^{-1} through the Swagelok cell. The cell was continuously ventilated for 6 h until the baseline was stable and then charged to 4.8 V versus Li/Li^+ at a current density of 15 mA g^{-1}, and held at 4.8 V versus Li/Li^+ for 4 h.

Data availability

The authors declare that all data supporting the findings of this study are available within the Article and its Supplementary Information files. Source data are provided with this paper.

References

1. Goodenough, J. B. & Kim, Y. Challenges for rechargeable Li batteries. *Chem. Mater.* **22**, 587–603 (2010).
2. Berg, E. J., Villevieille, C., Streich, D., Trabesinger, S. & Novak, P. Rechargeable batteries: grasping for the limits of chemistry. *J. Electrochem. Soc.* **162**, A2468–A2475 (2015).
3. Ahmed, S., Nelson, P. A., Gallagher, K. G., Susarla, N. & Dees, D. W. Cost and energy demand of producing nickel manganese cobalt cathode material for lithium-ion batteries. *J. Power Sources* **342**, 733–740 (2017).
4. Hirsh, H. S. et al. Sodium-ion batteries paving the way for grid energy storage. *Adv. Energy Mater.* **10**, 202001274 (2020).
5. Lee, J. et al. Unlocking the potential of cation-disordered oxides for rechargeable lithium batteries. *Science* **343**, 519–522 (2014).
6. Clement, R. J., Lun, Z. & Ceder, G. Cation-disordered rocksalt transition metal oxides and oxyfluorides for high energy lithium-ion cathodes. *Energ. Environ. Sci.* **13**, 345–373 (2020).
7. Ji, H. W. et al. Ultrahigh power and energy density in partially ordered lithium-ion cathode materials. *Nat. Energy* **5**, 213–221 (2020).

8. Lee, J. et al. Reversible Mn^{2+}/Mn^{4+} double redox in lithium-excess cathode materials. *Nature* **556**, 185 (2018).
9. Lun, Z. Y. et al. Cation-disordered rocksalt-type high-entropy cathodes for Li-ion batteries. *Nat. Mater.* **20**, 214 (2021).
10. Yabuuchi, N. et al. High-capacity electrode materials for rechargeable lithium batteries: Li_3NbO_4-based system with cation-disordered rocksalt structure. *Proc. Natl Acad. Sci. USA* **112**, 7650–7655 (2015).
11. Wang, R. et al. A disordered rocksalt Li-excess cathode material with high capacity and substantial oxygen redox activity: $Li_{1.25}Nb_{0.25}Mn_{0.5}O_2$. *Electrochem. Commun.* **60**, 70–73 (2015).
12. Xue, W. J. et al. Ultra-high-voltage Ni-rich layered cathodes in practical Li metal batteries enabled by a sulfonamide-based electrolyte. *Nat. Energy* **6**, 495–505 (2021).
13. Zhu, Z. et al. Gradient-morph $LiCoO_2$ single crystals with stabilized energy density above 3400 W h L^{-1}. *Energ. Environ. Sci.* **13**, 1865–1878 (2020).
14. Armstrong, A. R. et al. Demonstrating oxygen loss and associated structural reorganization in the lithium battery cathode $Li[Ni_{0.2}Li_{0.2}Mn_{0.6}]O_2$. *J. Am. Chem. Soc.* **128**, 8694–8698 (2006).
15. Yoon, M. et al. Unveiling nickel chemistry in stabilizing high-voltage cobalt-rich cathodes for lithium-ion batteries. *Adv. Funct. Mater.* **30**, 201907903 (2020).
16. Zhu, Z. et al. Gradient Li-rich oxide cathode particles immunized against oxygen release by a molten salt treatment. *Nat. Energy* **4**, 1049–1058 (2019).
17. Dong, Y., Liang, Q., Alvarez, A., Li, J. & Chen, I.-W. Enhanced mobility of cations and anions in the redox state: the polaronium mechanism. *Acta Mater.* **232**, 117941 (2022).
18. Yan, P. F. et al. Injection of oxygen vacancies in the bulk lattice of layered cathodes. *Nat. Nanotechnol.* **14**, 602 (2019).
19. Lee, J. et al. Determining the criticality of Li-excess for disordered-rocksalt Li-ion battery cathodes. *Adv. Energy Mater.* **11**, 2100204 (2021).
20. Hao Li, R. F. et al. Toward high-energy Mn-based disordered-rocksalt Li-ion cathodes. *Joule* **6**, 53–91 (2022).
21. Lee, E. S. & Manthiram, A. Smart design of lithium-rich layered oxide cathode compositions with suppressed voltage decay. *J. Mater. Chem. A* **2**, 3932–3939 (2014).
22. Christian, M., Julien, A. M., Zaghib, K. & Groult, H. Comparative issues of cathode materials for Li-ion batteries. *Inorganics* **2**, 132–154 (2014).
23. Radin, M. D. et al. Narrowing the gap between theoretical and practical capacities in Li-ion layered oxide cathode materials. *Adv. Energy Mater.* **7**, 201602888 (2017).
24. Zhang, W. J. Structure and performance of $LiFePO_4$ cathode materials: a review. *J. Power Sources* **196**, 2962–2970 (2011).
25. Manthiram, A. & Goodenough, J. B. Lithium-based polyanion oxide cathodes. *Nat. Energy* **6**, 844–845 (2021).
26. Manthiram, A. A reflection on lithium-ion battery cathode chemistry. *Nat. Commun.* **11**, 1–9 (2020).
27. Sawamura, M. et al. Nanostructured $LiMnO_2$ with Li_3PO_4 integrated at the atomic scale for high-energy electrode materials with reversible anionic redox. *ACS Cent. Sci.* **6**, 2326–2338 (2020).
28. House, R. A. et al. Superstructure control of first-cycle voltage hysteresis in oxygen-redox cathodes. *Nature* **577**, 502–508 (2020).
29. Sumita, M., Tanaka, Y., Ikeda, M. & Ohno, T. Theoretically designed Li_3PO_4 (100)/$LiFePO_4$ (010) coherent electrolyte/cathode interface for all solid-state Li-ion secondary batteries. *J. Phys. Chem. C* **119**, 14–22 (2015).
30. Gnewuch, S. & Rodriguez, E. E. Distinguishing the intrinsic antiferromagnetism in polycrystalline $LiCoPO_4$ and $LiMnPO_4$ olivines. *Inorg. Chem.* **59**, 5883–5895 (2020).
31. Chung, H. T., Myung, S. T., Cho, T. H. & Son, J. T. Lattice parameter as a measure of electrochemical properties of $LiMn_2O_4$. *J. Power Sources* **97**, 454–457 (2001).
32. Li, T., Chang, K., Hashem, A. M. & Julien, C. M. Structural and electrochemical properties of the high Ni-content spinel $LiNiMnO_4$. *Electrochem* **2**, 95–117 (2021).
33. Akimoto, J. & Gotoh, Y. Single crystal growth, structure and physical property of $LiCoO_2$ and $LiNiO_2$. *Mol. Cryst. Liq. Cryst.* **341**, 947–950 (2000).
34. de Biasi, L. et al. Chemical, structural, and electronic aspects of formation and degradation behavior on different length scales of Ni-rich NCM and Li-rich HE-NCM cathode materials in Li-ion batteries. *Adv. Mater.* **31**, 201900985 (2019).
35. Markevich, E. et al. Raman spectroscopy of carbon-coated $LiCoPO_4$ and $LiFePO_4$ olivines. *J. Power Sources* **196**, 6433–6439 (2011).
36. Julien, C. M. & Massot, M. Lattice vibrations of materials for lithium rechargeable batteries. III. Lithium manganese oxides. *Mater. Sci. Eng. B* **100**, 69–78 (2003).
37. Wu, J. et al. In situ Raman spectroscopy of $LiFePO_4$: size and morphology dependence during charge and self-discharge. *Nanotechnology* **24**, 424009 (2013).
38. Tang, D. et al. Electrochemical behavior and surface structural change of $LiMn_2O_4$ charged to 5.1 V. *J. Mater. Chem. A* **2**, 14519–14527 (2014).
39. Tang, D. et al. Surface structure evolution of $LiMn_2O_4$ cathode material upon charge/discharge. *Chem. Mater.* **26**, 3535–3543 (2014).
40. Manceau, A., Marcus, M. A. & Grangeon, S. Determination of Mn valence states in mixed-valent manganates by XANES spectroscopy. *Am. Mineral.* **97**, 816–827 (2012).

Acknowledgements

We acknowledge funding by Honda Research Institute USA, Inc. This research used resources of 7-BM of the National Synchrotron Light Source II, a US Department of Energy (DOE) Office of Science User Facility operated for the DOE Office of Science by Brookhaven National Laboratory under contract no. DE-SC0012704. The authors acknowledge support by the Molecular Foundry at Lawrence Berkeley National Laboratory (LBNL), which is supported by the US Department of Energy under contract no. DE-AC02-05-CH11231. This research used resources of the Advanced Photon Source (11-BM and 11-ID-B), a US Department of Energy (DOE) Office of Science User Facility operated for the DOE Office of Science by Argonne National Laboratory under contract no. DE-AC02-06CH11357. This research used resources of the 17B and 16U1 beamlines of Shanghai Synchrotron Radiation Facility. Y.Y., Y.S. and Y. Han thank the support from the Institutes of Energy and the Environment (IEE) Seed Grant Program at The Pennsylvania State University.

Author contributions

Y. Huang, Y.D. and J. Li. conceived the project. Y. Huang synthesized the materials and conducted XRD, SEM, ICP-OES and XRF measurements. Y. Huang, M.Y., S.L., E.Y.Z., Y.L. and H.J. contributed to electrochemical testing. Y.Y., Y.S., Y. Han, J.C., C.O., C.S. and A.P. contributed to sample preparations, data collection and data processing for HAADF-STEM and EELS. T.L. contributed to high-resolution XRD and PDF measurements. W.H.K., H.C. and W.Y. contributed to neutron powder diffraction measurements. Y.P. and M.L. contributed to DEMS measurements. B.W. contributed to TEM imaging, SAED and STEM–EDS. B.W., Z.C., Y.Z. and H.J. contributed to Raman measurements. Z.C. and J.X contributed to ICP-MS measurements. L.M., X.X. and L.G. contributed to XANES measurements. W.L., R.M. and C.Y. contributed to XRD Rietveld

refinement. Y. Huang and Y.D. analysed the data. Y. Huang, Y.D. and J. Li. wrote the paper. All authors discussed and contributed to the writing.

Competing interests

Y. Huang, Y.D. and J. Li report a US non-provisional patent application filed by the Massachusetts Institute of Technology, patent application no. 18/790,946. The patent is related to the compositions and synthesis method reported in this Article. The other authors declare no competing interests.

Additional information

Supplementary information The online version contains supplementary material available at https://doi.org/10.1038/s41560-024-01615-6.

Correspondence and requests for materials should be addressed to Yanhao Dong or Ju Li.

Peer review information *Nature Energy* thanks Wei Kong Pang and the other, anonymous, reviewer(s) for their contribution to the peer review of this work.

[1]Department of Materials Science and Engineering, Massachusetts Institute of Technology, Cambridge, MA, USA. [2]State Key Laboratory of New Ceramics and Fine Processing, School of Materials Science and Engineering, Tsinghua University, Beijing, China. [3]Department of Nuclear Science and Engineering, Massachusetts Institute of Technology, Cambridge, MA, USA. [4]Department of Engineering Science and Mechanics and Materials Research Institute, The Pennsylvania State University, University Park, PA, USA. [5]Chemical Sciences and Engineering Division, Argonne National Laboratory, Argonne, IL, USA. [6]Department of Chemical and Biological Engineering, Gachon University, Seongnam-si, Republic of Korea. [7]Department of Mining and Materials Engineering, McGill University, Montréal, Quebec, Canada. [8]National Center for Electron Microscopy, Molecular Foundry, Lawrence Berkeley National Laboratory, Berkeley, CA, USA. [9]MIT.Nano, Massachusetts Institute of Technology, Cambridge, MA, USA. [10]Department of Materials Science and Engineering, Huazhong University of Science and Technology, Wuhan, China. [11]Department of Chemistry, Department of Materials Science, Shanghai Key Laboratory of Molecular Catalysis and Innovative Materials, Fudan University, Shanghai, China. [12]National Synchrotron Light Source II, Brookhaven National Laboratory, Upton, NY, USA. [13]Spallation Neutron Source Science Center, Dongguan, China. [14]Institute of High Energy Physics, Chinese Academy of Sciences, Beijing, China. [15]Shanghai Synchrotron Radiation Facility, Shanghai Advanced Research Institute, Chinese Academy of Sciences, Shanghai, China. [16]Department of Chemical Engineering, R&D Center for Membrane Technology, Center for Circular Economy, Chung Yuan Christian University, Taoyuan City, Taiwan ROC. [17]Department of Physics, National Central University, Taoyuan City, Taiwan ROC. ✉e-mail: dongyanhao@tsinghua.edu.cn; liju@mit.edu

nature energy

Supplementary information

https://doi.org/10.1038/s41560-024-01615-6

Integrated rocksalt–polyanion cathodes with excess lithium and stabilized cycling

In the format provided by the authors and unedited

Table of contents

Supplementary Note 1 | Design principles on materials and stoichiometry.

The chemistry $Li_{2+u-v}M_{2-u}[XO_4]_xO_{4(1-x)}$ for high capacity/energy density, bulk polyanion (XO_4 group, X = P, Si, S, B) incorporation and stabilized lattice oxygen for synthesizable DRXPS cathodes were designed with the following considerations:

1. Cation filling: With an FCC oxygen framework, we assume octahedral site occupancy for *M*, tetrahedral or octahedral site occupancy for Li, and tetrahedral site occupancy for *X* (this holds for P, Si and S, and is a simplification for B as it may also form trigonal planar BO_3[1]).

2. Spinel-type transition metal ordering: A spinel-type *M* ordering (**Supplementary Figure 22a**) is preferred to fully utilize *M* 3*d* - O 2*p* hybridization to stabilize the oxygen framework and to provide 3-dimensional (3D) channels for Li^+ diffusion[2]. This can be realized in a spinel structure with LiM_2O_4 stoichiometry, a rocksalt structure with $Li_{[16c]}M_{[16d]}O_2$ stoichiometry, or their composites.

3. Cation deficiency: To successfully incorporate polyanions into the lattice, the four octahedral sites face-shared with an XO_4 tetrahedron should be empty (**Supplementary Figure 22b**). Thus, in synthesis, one should make sure that $4x \leq 4 - (2+u-v) - (2-u)$ or $x_{max} = v/4$ for a given v. In charging, v increases ($v_{max} = 2+u$), and in discharging, v decreases but there is always a lower bound: $v_{min} = 4x$ for a given x.

4. O stabilization: Oxide ions can be classified into stable bonded oxygen (O_B) and labile underbonded oxygen (O_{UB}). O_B is considered as O bonded to three *M* cations in an octahedral complex (O-3*M*) or O belonging to the polyanion group (O-*X*, regardless of the number of *M* neighbors), and O_{UB} are O-2*M*, O-1*M* or O-0*M* (**Supplementary Figure 23**). For effective stabilization of HACR cathodes without long-range O diffusion/loss, O_{UB} needs to be non-percolating in the anion sublattice. The percolation threshold for an 3D FCC lattice is 0.2[3,4], and thus the O_{UB} ratio should be below 20% (or O_B ratio > 80%).

5. *M*/O ratio, *m*: To enable high capacity and energy density, there should be sufficient high-symmetry lattice sites for full lithiation (**Figure 1b**). Assuming that anion redox is active and the neighboring octahedral sites of an XO_4 tetrahedron can be electrochemically lithiated, the theoretical capacity of $Li_{2+u-v}M_{2-u}[XO_4]_xO_{4(1-x)}$ is limited by the M content only, as a maximum of (2+*u*) Li can be inserted. For layered cathodes $LiMO_2$ (*M* = Ni/Co/Mn, $u = 0$), the theoretical capacity is around 280 mAh g^{-1}, with $v_{min} = 0$. To reach higher capacities, one needs $u > 0$ (also reduces molecular weight per formula unit). However, increasing *u* sacrifices the stability of the M-O framework with less O_B (only considering O-3*M* for O_B and O-2*M* for O_{UB}, then O_B ratio = 6*m*–2, where $m = \frac{2-u}{4}$ for cathodes without polyanion solid solution, black line in **Supplementary Figure 24**). The O_B ratio is only 0.4 for the stoichiometry,

$Li_{1.2}M_{0.8}O_2$, of conventional Li-rich layered cathodes, which might explain their performance decay. Increasing u also increases the average M valence. For as-synthesized cathodes, Mn and Fe typically have a valence no more than +4 and +3, respectively, beyond which it is too oxidizing to be stable in air. These give an upper bound for u.

6. X/O ratio: The motivation for polyanion solid solution is to stabilize lattice oxygen and increase high voltage cyclability. As X strongly binds to its four first-nearest O via covalent bond, forming the XO_4 polyanion group in $M_{2-u}[XO_4]_xO_{4(1-x)}$, the effective M/O ratio, $m = \frac{2-u}{4-4x}$, is larger compared to the polyanion-free $M_{2-u}O_4$ with $m = \frac{2-u}{4}$, meaning a more robust structure with fewer labile O_{UB} (**Figure 1c**). For effective stabilization with O_{UB} ratio kept below 0.2, a lower bound for x should exist, which is estimated in the following two limiting cases. (i) Without considering P-Li interactions and assuming evenly spaced Li and M at 16d sites and X at 8a sites, O_{UB} should only consist of O-2M, and O_B consists of O-3M and O-X. Let p be the population of a certain O configuration per formula unit $Li_{2+u-v}M_{2-u}[XO_4]_xO_{4(1-x)}$, then we have $p_{O-3M} = (6m-2)(4-4x)$ and $p_{O-X} = 4x$, and $p_{O_B} = p_{O-3M} + p_{O-X} \geq 4(1-0.2)$ is required for stability. Solving for x we obtain $x_{min,i} = 0.5u - 0.067$. In reality, we may have certain amounts of O-1M or O-0M if Li/M short-range ordering (SRO) is considered, since the polyanion element with high positive valence prefers Li^+ over $Mn^{3+/4+}$ in its proximity to minimize electrostatic repulsion. This makes $p_{O-3M} > (6m-2)(4-4x)$ and thus a lower $x_{min,i}$. (ii) Assuming strong SRO between X and Li, i.e., all u 16d Li octahedra are corner-shared with X tetrahedra (assuming the total number of 16d octahedra corner-shared with X tetrahedra, $12x$, is greater than u, which is likely the case), then $p_{O-0M} = 0$ and $p_{O-1M} = u/2$. Since $p_{O-1M} + p_{O-2M} + p_{O-3M} = 4-4x$ and $p_{O-1M} + 2p_{O-2M} + 3p_{O-3M} = 6m$, we can solve $p_{O-3M} = 4 + 8x - 5.5u$. Also, we have $p_{O-X} = 4x$ and $p_{O_B} = p_{O-3M} + p_{O-X} \geq 4(1-0.2)$. Solving for x we obtain $x_{min,ii} = 0.458u - 0.067$. The true x_{min} should lie between these two minima. Note that due to minor cation disorder between Mn at 16d and 16c sites (~7% Mn at 16c sites for $Li_{1.67}Mn_{1.5}P_{0.17}O_4$ from **Supplementary Table 2**), there is a small possibility of Li-O-Li configuration in O-3M' complexes with Mn at 16c site (**Supplementary Figure 23**, bottom left), which can also lead to labile oxygen states. If we set f to be the fraction of Mn at 16c sites ($f = \frac{n_{Mn[16c]}}{n_{Mn[16c]}+n_{Mn[16d]}}$, n is the number of moles). We denote the revised parameters with ' (prime symbol). The effective M/O ratio is then $m' = m \cdot (1-f) = \frac{2-u}{4-4x}(1-f)$, and we obtain $x'_{min,i} = 0.5u - 0.067 + (1-0.5u)f = x_{min,i} + (1-0.5u)f$ and $x'_{min,ii} = 0.458u - 0.067 + (1-0.5u)f = x_{min,ii} + (1-0.5u)f$. This calculation is a bit overshot since there is a small chance that all three 16c sites adjacent to an oxygen atom are occupied by Mn, which is a stabilized oxygen configuration, and thus the values should be between x and x'. The limits of x (assuming no cation disorder, i.e., Mn at 16c sites) are plotted in **Supplementary Figure 25a**. For studying varying P content, x, in $Li_{1.67}Mn_{1.67-x}P_xO_4$, we plug in $u = x +$

0.33 and $v = x + 0.67$ into the above equations, and obtain $x_{min,i} = 0.2$, $x_{min,ii} = 0.159$, and $x_{max} = 0.222$. The range $0.159 < x < 0.222$ is marked on **Supplementary Figure 18c-d**, matching the best-performing compositions.

7. The previous discussions assumed that Li^+ can only take octahedral cation sites in DRX. In reality, Li^+ can also take tetrahedral sites, represented by t in $Li_{2+u-v+t}M_{2-u}[XO_4]_xO_{4(1-x)}$. As shown in the following sections, lithiation can proceed beyond $(2+u-v_{min})$ Li towards the end of discharge, indicating tetrahedral occupations of Li at lower voltages (< 2.3 V vs. Li/Li^+), and a larger theoretical capacity than only considering octahedral Li occupation (the blue line in **Supplementary Figure 24** is drawn by assuming $v_{min}–t_{max} = (v–t)_{min} = x$, which is a reasonable estimate since we lithiated to $v–t = 1.38x$ in **Figure 3b**). We should distinguish these t tetrahedral sites from the $2+u−v$ octahedral sites. Note that $t > 0$ becomes significant only at low voltages, and thus does not enter the high-voltage O sublattice discussion much. In **Figure 3b**, we mark the theoretical capacity with dashed lines under the two assumptions: Li tetrahedral occupation is not allowed (green dashed line), estimated with $(v–t)_{min} = x$; Li tetrahedral occupation is allowed (blue dashed line), estimated with $(v–t)_{min} = 4x$.

Based on the discussions, we see that polyanion solid solution (blue line in **Supplementary Figure 24**) grants larger capacity compared to polyanion-free compositions with the same O_B ratio (similar reversibility), and higher O_B ratio (better reversibility) than the polyanion-free composition with similar capacity.

Supplementary Note 2 | Detailed study of $Li_{1.67}Mn_{1.5}P_{0.17}O_4$ stability and comparison with $Li_{1.67}Mn_{1.5}Nb_{0.17}O_4$. We performed additional experiments to study the stability of $Li_{1.67}Mn_{1.5}P_{0.17}O_4$ and comparison with $Li_{1.67}Mn_{1.5}Nb_{0.17}O_4$, which further illustrates the superior stabilizing effects of the polyanion solid-solution strategy. First, we performed ex situ XRD measurement on the cathode film after cycling (**Supplementary Figure 26**). Ex situ XRD data shows that the spinel structure is maintained after 100 cycles, indicating good structural stability. Second, we performed in situ differential electrochemical mass spectroscopy (DEMS) measurement (**Supplementary Figure 14**) on the first charge cycle of the cathodes, which shows much less gas evolution (CO_2 and O_2) for $Li_{1.67}Mn_{1.5}P_{0.17}O_4$. Third, we performed inductively coupled plasma optical emission spectroscopy (ICP-OES) on the electrolyte soaked with cathode film after cycling (**Supplementary Figure 15a**), and X-ray fluorescence (XRF) on the lithium anode after cycling (**Supplementary Figure 15b**). Both ICP-OES and XRF measurements reveal that the $Li_{1.67}Mn_{1.5}P_{0.17}O_4$ cell experiences less Mn dissolution from the cathode than the $Li_{1.67}Mn_{1.5}Nb_{0.17}O_4$ cell upon cycling. Lastly, we cycled $Li_{1.67}Mn_{1.5}P_{0.17}O_4$ under different voltage windows (**Supplementary Figure 27**) and observed similar retention rates when we lower the upper cutoff voltage (72% at 4.8 V, 70% at 4.7 V, 69% at 4.6 V, and 70% at 4.4 V, all vs. Li/Li^+ and over 100 cycles) and increase the lower cutoff voltage (72% at 1.5 V, 63% at 2.0 V, 74% at 2.5 V, all vs. Li/Li^+ and over 100 cycles). This shows that $Li_{1.67}Mn_{1.5}P_{0.17}O_4$ is robust against degradations under extreme electrochemical conditions. These experiments all point to the significant improvement to both the bulk structural stability and the surface chemical stability by the introduction of polyanions.

Supplementary Note 3 | Study of base compositions with varying *u* and *v*.

Supplementary Figure 25b shows the projection of x in **Supplementary Figure 25a** onto its x-y plane, which reflects different regimes of polyanion stabilization for different base compositions. In the red-colored region where $x_{max} < 0$, it is impossible to even synthesize phase-pure polyanionic compositions due to the lack of cation deficiency for the incorporation of polyanion groups. In the yellow-colored region where $0 < x_{max} < x_{min}$, the maximum allowed polyanion content for phase-pure synthesis is not sufficient to ensure non-percolating labile underbonded oxygen (O_{UB}). It is desirable to choose a base composition $Li_{2+u-v}M_{2-u}O_4$ in the blue-colored region with $0 < x_{min} < x_{max}$. For verification, we studied compositions with varying u and v (all synthesized compositions marked in **Supplementary Figure 25b**).

We first varied the Li content and thus cation deficiency in $Li_{2.5-v}Mn_{1.5}P_{0.17}O_4$ (v = –0.17, 0.17, 0.5, 0.83, 1.17) while fixing the amounts of Mn (u = 0.5) and P (x = 0.17) (**Supplementary Figure 28**). We found that a high level of cation deficiency with $0.5 \leq v \leq 1.17$ is critical to the formation of the spinel phase (**Supplementary Figure 28a**), while larger v (less cation deficiency) results in rocksalt-type phase and eliminates the spinel-type cation ordering. We then cycled $Li_{2.5-v}Mn_{1.5}P_{0.17}O_4$ between 1.5 – 4.8 V vs. Li/Li^+ at 50 mA g^{-1}, after two formation cycles at 20 mA g^{-1}. As shown in **Supplementary Figure 28b**, while all polyanionic compositions show good cycling stability, the spinel-phase $Li_{2.5-v}Mn_{1.5}P_{0.17}O_4$ (v = 0.5, 0.83, 1.17) leads to higher discharge energy density than the rocksalt ones (v = –0.17 and 0.17). The 25th-cycle discharge energy densities are in the range of 830-890 Wh kg^{-1} for the spinel phases (**Supplementary Figure 28c**), which are higher than the rocksalt ones and the 730 Wh kg^{-1} benchmark. This proves the importance of the spinel phase and cation deficiency upon synthesis, as proposed in the design principles.

We then varied the effective M/O ratio, $m = \frac{2-u}{3.12+0.44u}$, in $Li_{1.17+u}Mn_{2-u}P_{0.22-0.11u}O_4$ (u = 0.2, 0.35, 0.5, 0.65, 0.8) such that the cation deficiency (v = 0.83) and spinel order (molar ratio n_{Li+M}/n_O = 0.79) are fixed (**Supplementary Figure 29**). While all compositions exhibit a spinel-like phase (**Supplementary Figure 29a**), their cycling performances differ. Compositions with intermediate u (u = 0.35, 0.5 and 0.65, especially u = 0.5) show the best cycling stability with high initial energy densities. The composition with u = 0.2 shows a lower initial energy density but good cycling stability, and the composition with u = 0.8 has a slightly larger initial energy density (larger than u = 0.2 but still smaller than others since Mn valence is > +4 by design for u = 0.8) but the worst cycling stability (**Supplementary Figure 29b**). Their 25th-cycle discharge energy densities show a volcano-type relation with respect to u (**Supplementary Figure 29c**). This justifies the design principle that the M/O ratio should be a compromise between capacity and structural stability (while ensuring phase-pure synthesis). Generally speaking, to achieve high

capacity and energy density, an effective *M*/O ratio down to 0.4 (**Supplementary Figure 29c**) can be accepted that does not sacrifice cycling stability too much. This is between that of layered LiMO$_2$ (m = 0.5) and Li-rich Li$_2$MnO$_3$ (m = 0.33).

Supplementary Note 4 | Towards more scalable mechanochemical synthesis of DRXPS.

Metastable materials such as DRXPS and other common disordered rocksalt cathodes are mostly synthesized with mechenochemical methods. Since high-energy planetary ball milling is energy-intensive and generally has a low product yield, making it commercially impractical, we tried synthesizing DRXPS at lower milling speeds. We performed milling at 400, 300, and 200 rpm for different durations, and found that DRXPS does form at lower milling speeds, but requires longer milling duration to achieve phase purity. From XRD patterns in **Supplementary Figure 30a**, we found that the desired phase without obvious impurity phases can be achieved with milling speed as low as 300 rpm if the milling duration is long enough (~60 hours). But there is a lower speed limit: if we further reduce the milling speed to 200 rpm, the speed at which is more common for simple physical mixing rather than mechanochemical synthesis, the desired phase cannot be formed even for a very long milling duration. The electrochemical performance does not change much when low milling speed is used for synthesis (**Supplementary Figure 30b**). This shows the feasibility of using a lower milling speed (300 rpm) to synthesize DRXPS cathodes, and such tolerant mechanochemical synthesis conditions for DRXPS can potentially lead to much higher product yields and lower costs. A lower milling speed means that larger ball milling jars with larger volumes can be used in planetary ball mills. For example, a planetary ball mill with a maximum speed of 390 rpm can hold four 10-liter jars, which is ~25× the volume of our benchtop high-energy ball mill with maximum speed of 1100 rpm. DRXPS can be produced on the kilogram-scale per batch at 300 – 400 rpm in the lab. In addition, other types of mills such as vibration, attrition, or tumbler mills can be utilized under such milling speeds, and these are typically much larger and more commercially available than planetary ball mills.

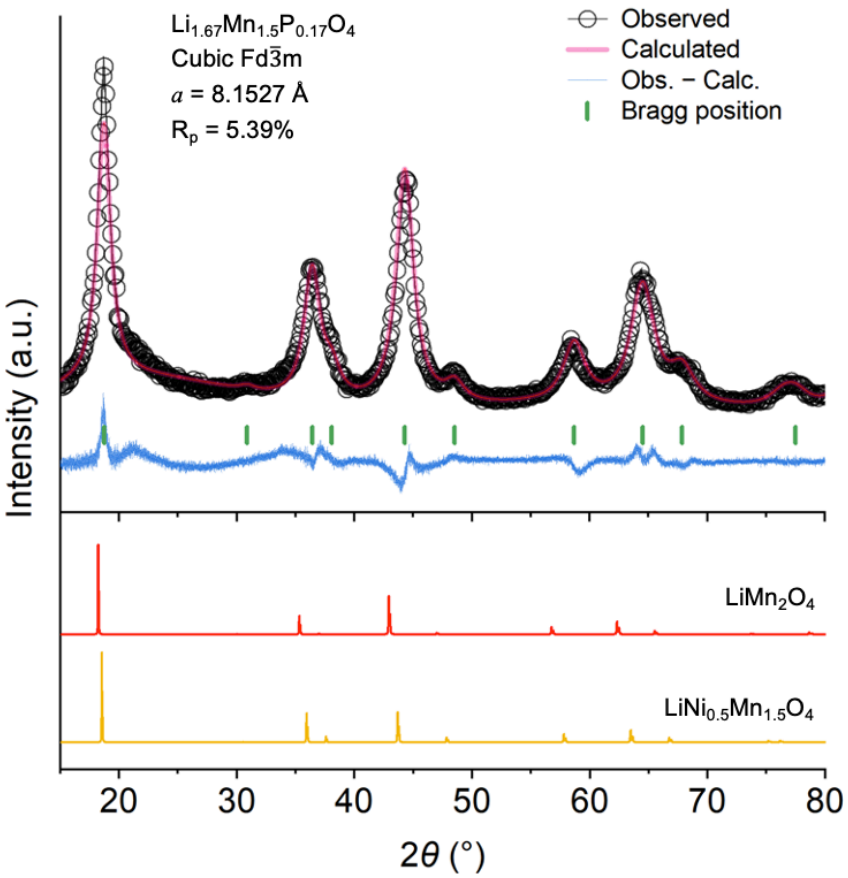

Supplementary Figure 1 | High-resolution XRD and Rietveld refinement of $Li_{1.67}Mn_{1.5}P_{0.17}O_4$. Refinement is performed using the GSAS II software. Refined parameters are shown in Supplementary Table 2. Spinel $LiMn_2O_4$ and $LiNi_{0.5}Mn_{1.5}O_4$ are shown as references.

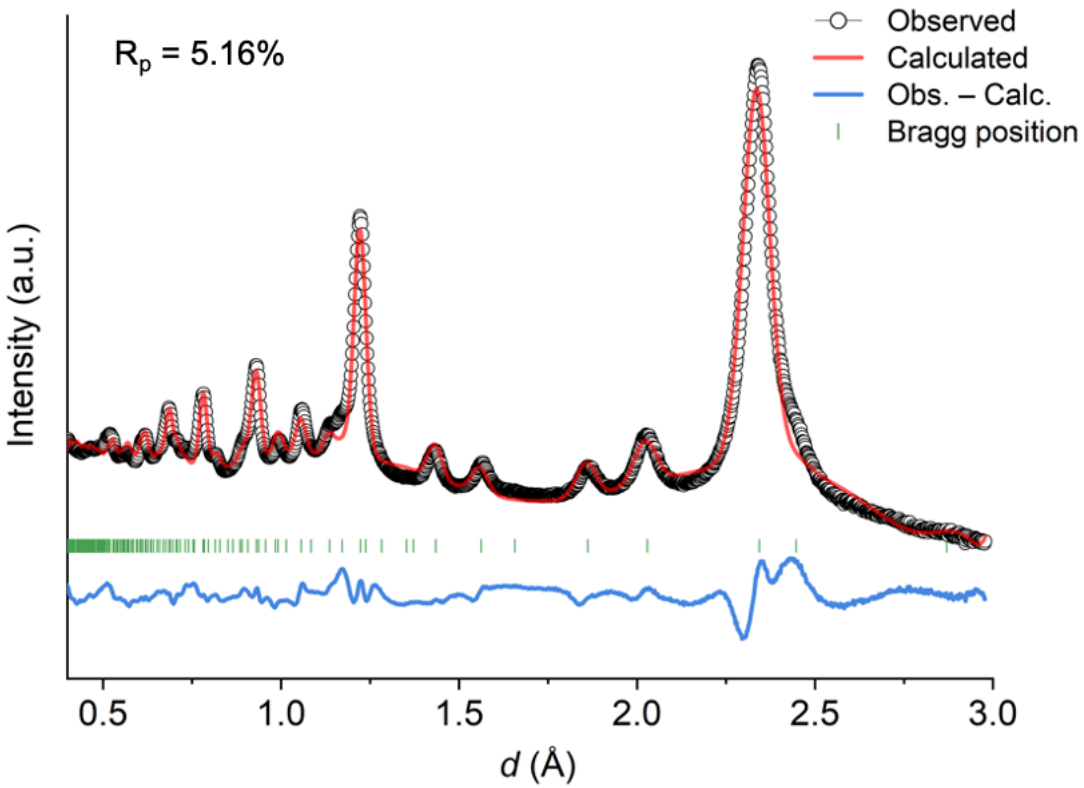

Supplementary Figure 2 | Neutron powder diffraction and Rietveld refinement of $Li_{1.67}Mn_{1.5}P_{0.17}O_4$. Refinement is performed using the GSAS II software. Refinement input is taken as the output from XRD refinement.

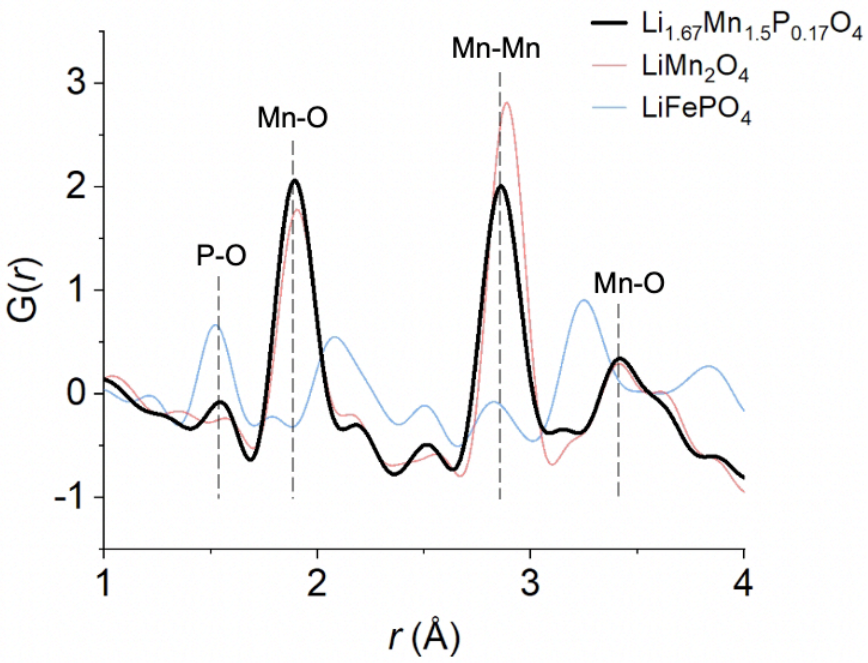

Supplementary Figure 3 | Pair distribution function measurement of $Li_{1.67}Mn_{1.5}P_{0.17}O_4$, $LiMn_2O_4$, and $LiFePO_4$. Peaks corresponding to atom pairs in $Li_{1.67}Mn_{1.5}P_{0.17}O_4$ are marked.

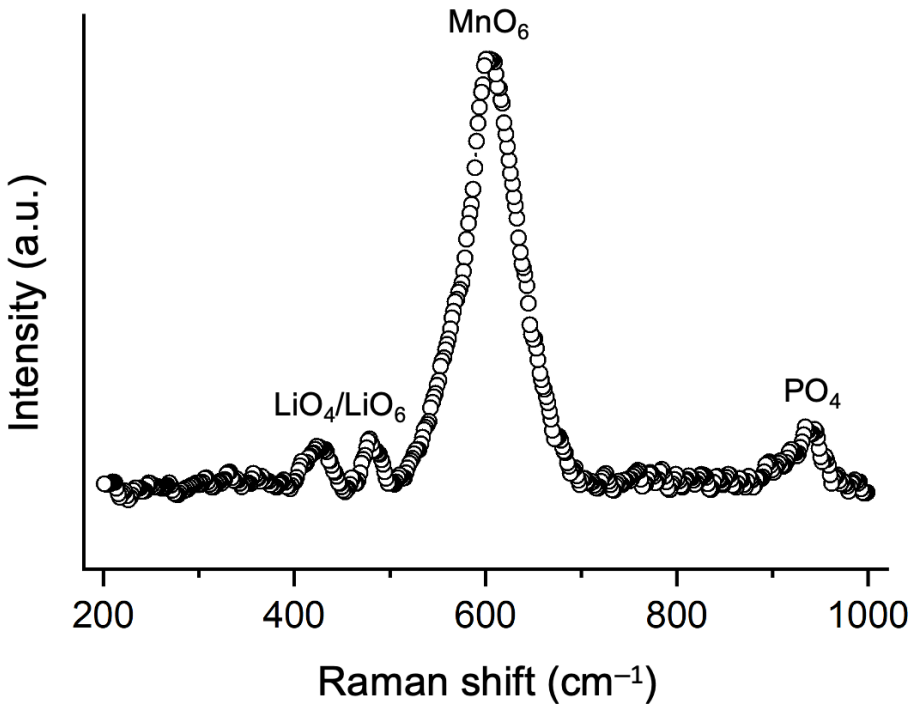

Supplementary Figure 4 | Raman measurement of $Li_{1.67}Mn_{1.5}P_{0.17}O_4$. Peaks are marked by their corresponding bonds.

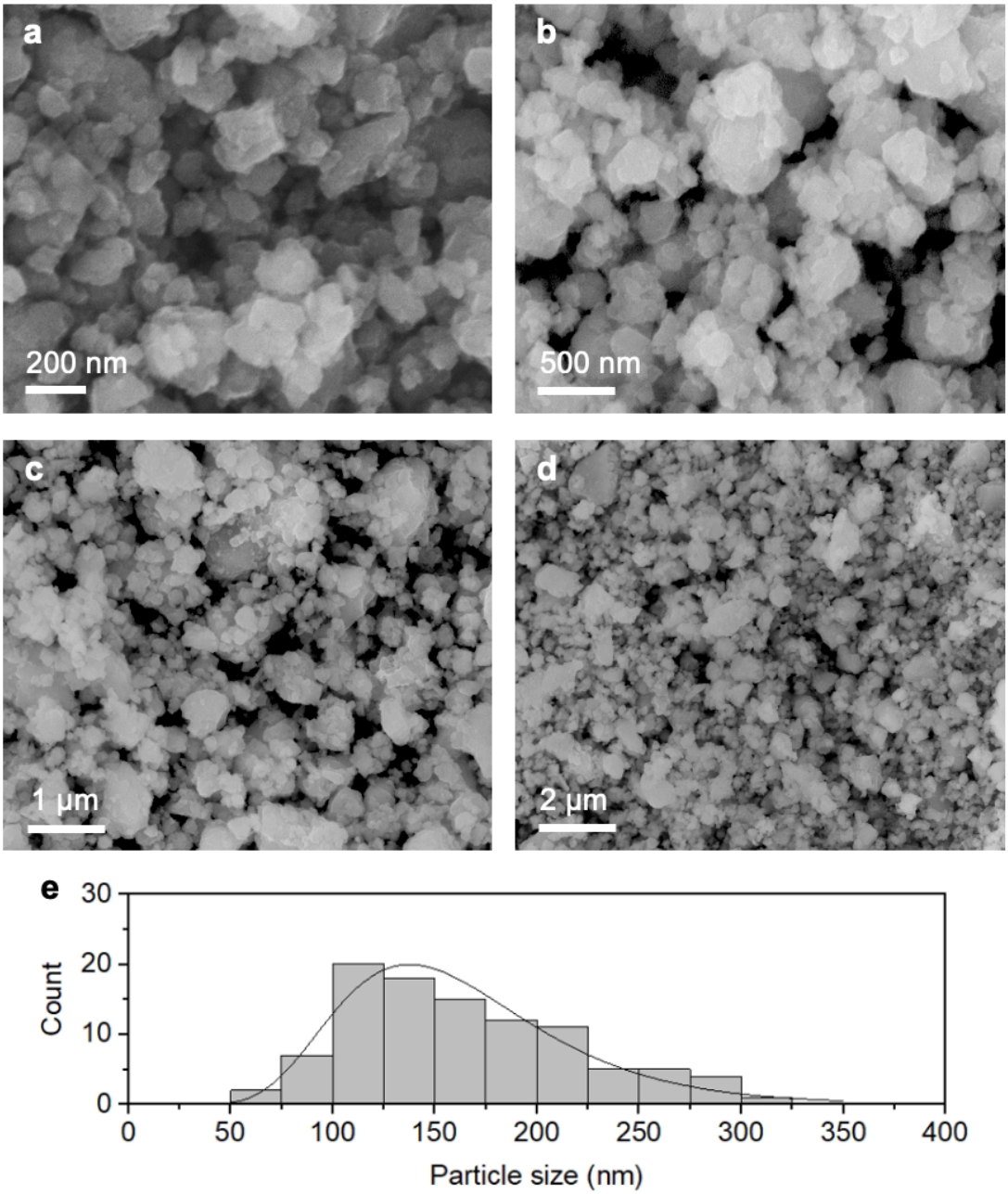

Supplementary Figure 5 | SEM image and particle size distribution of $Li_{1.67}Mn_{1.5}P_{0.17}O_4$ (ball-milled at 800 rpm for 5 h). a-d, SEM images taken at magnifications of (a) 30,000×, (b) 20,000×, (c) 10,000×, and (d) 5,000×. **e,** Particle size distribution analyzed from (b). 100 particles were sampled.

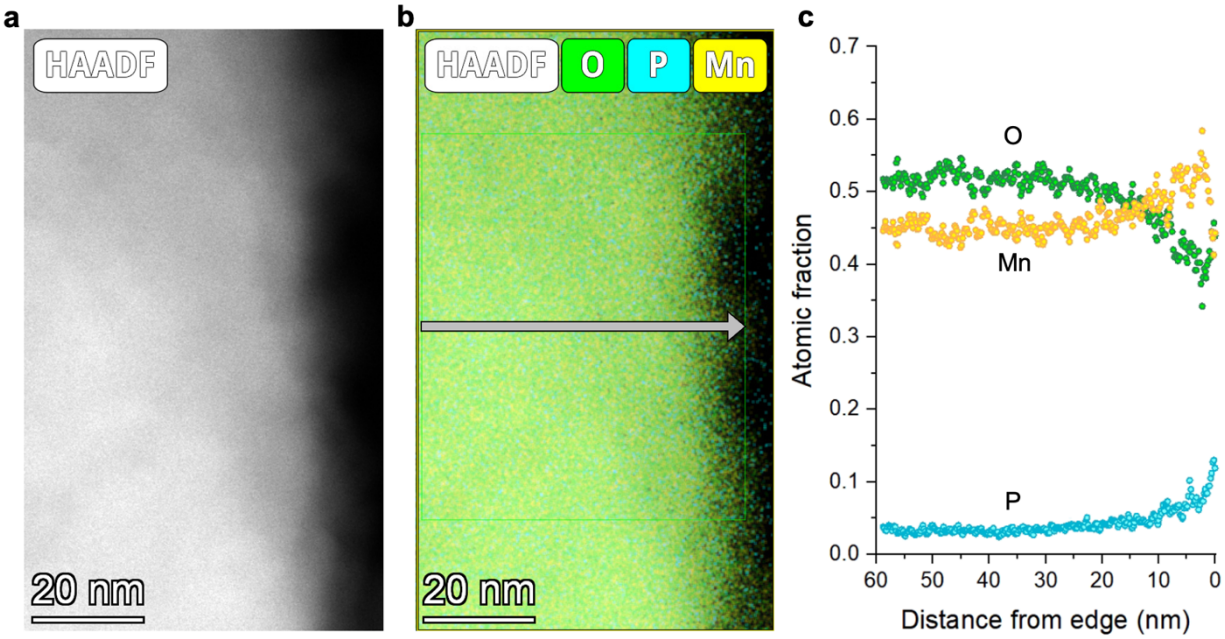

Supplementary Figure 6 | STEM-EDS mapping of $Li_{1.67}Mn_{1.5}P_{0.17}O_4$. a,b, STEM-EDS mapping of Mn, P and O performed on a larger region than Figure 2f. **c,** Line profile of Mn, P and O along the arrow indicated in (b). Note that the profile near the particle edge is affected by thickness effect, and should be disregarded. The profile away from the particle edge shows homogenous distribution of Mn, P and O.

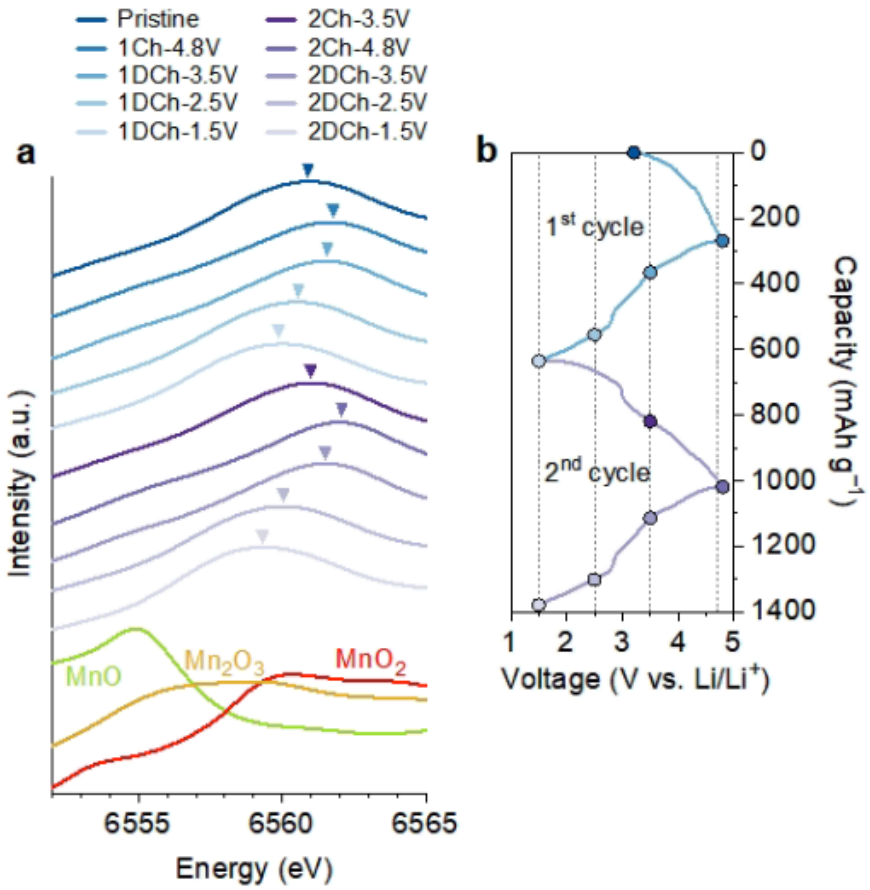

Supplementary Figure 7 | Ex situ XANES measurement of $Li_{1.67}Mn_{1.5}P_{0.17}O_4$. a, Mn K-edge XANES spectra of $Li_{1.67}Mn_{1.5}P_{0.17}O_4$ in the first two cycles, and MnO, Mn_2O_3 and MnO_2 references. **b,** Points along the voltage profile for $Li_{1.67}Mn_{1.5}P_{0.17}O_4$ at which ex situ XANES samples are taken.

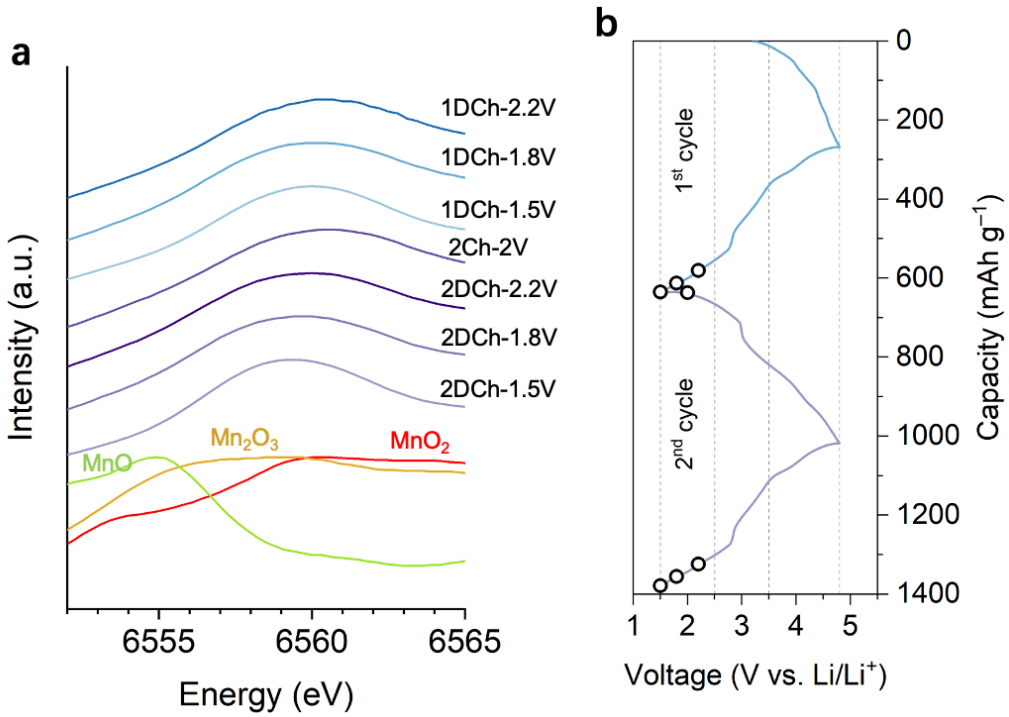

Supplementary Figure 8 | Ex situ XANES measurement of $Li_{1.67}Mn_{1.5}P_{0.17}O_4$ in the low voltage region (<2.5 V vs. Li/Li$^+$). a, Mn K-edge XANES spectra of $Li_{1.67}Mn_{1.5}P_{0.17}O_4$ in the first two cycles, and MnO, Mn_2O_3 and MnO_2 references. **b,** Points along the voltage profile for $Li_{1.67}Mn_{1.5}P_{0.17}O_4$ at which ex situ XANES samples are taken.

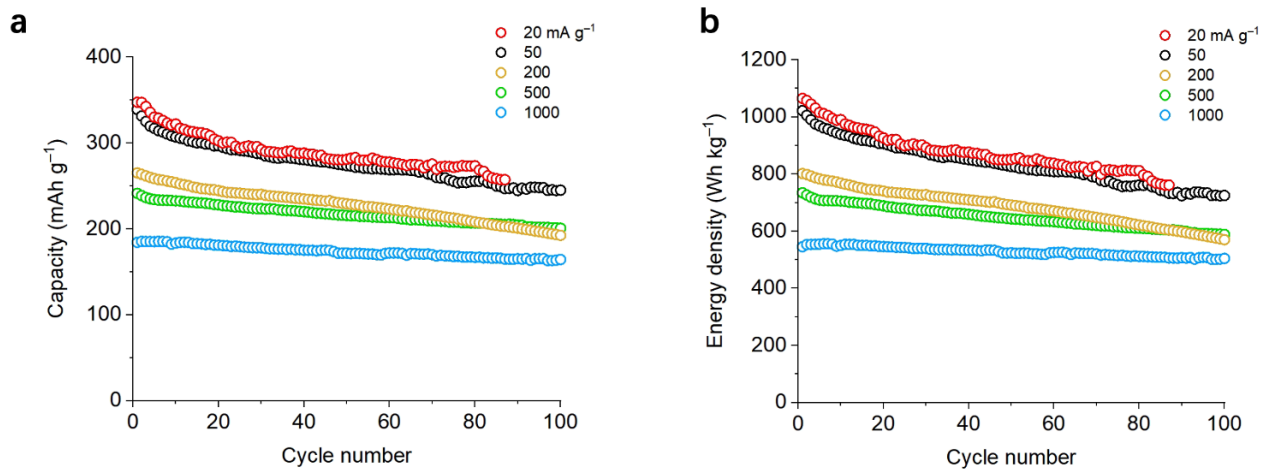

Supplementary Figure 9 | Cycling performance of $Li_{1.67}Mn_{1.5}P_{0.17}O_4$ at different current densities. a, Discharge capacity and **b,** discharge energy density retention when cycled between 1.5 – 4.8 V vs. Li/Li^+ at 20, 50, 200, 500, and 1000 mA g^{-1}, all following two initial formation cycles at 20 mA g^{-1} (not shown).

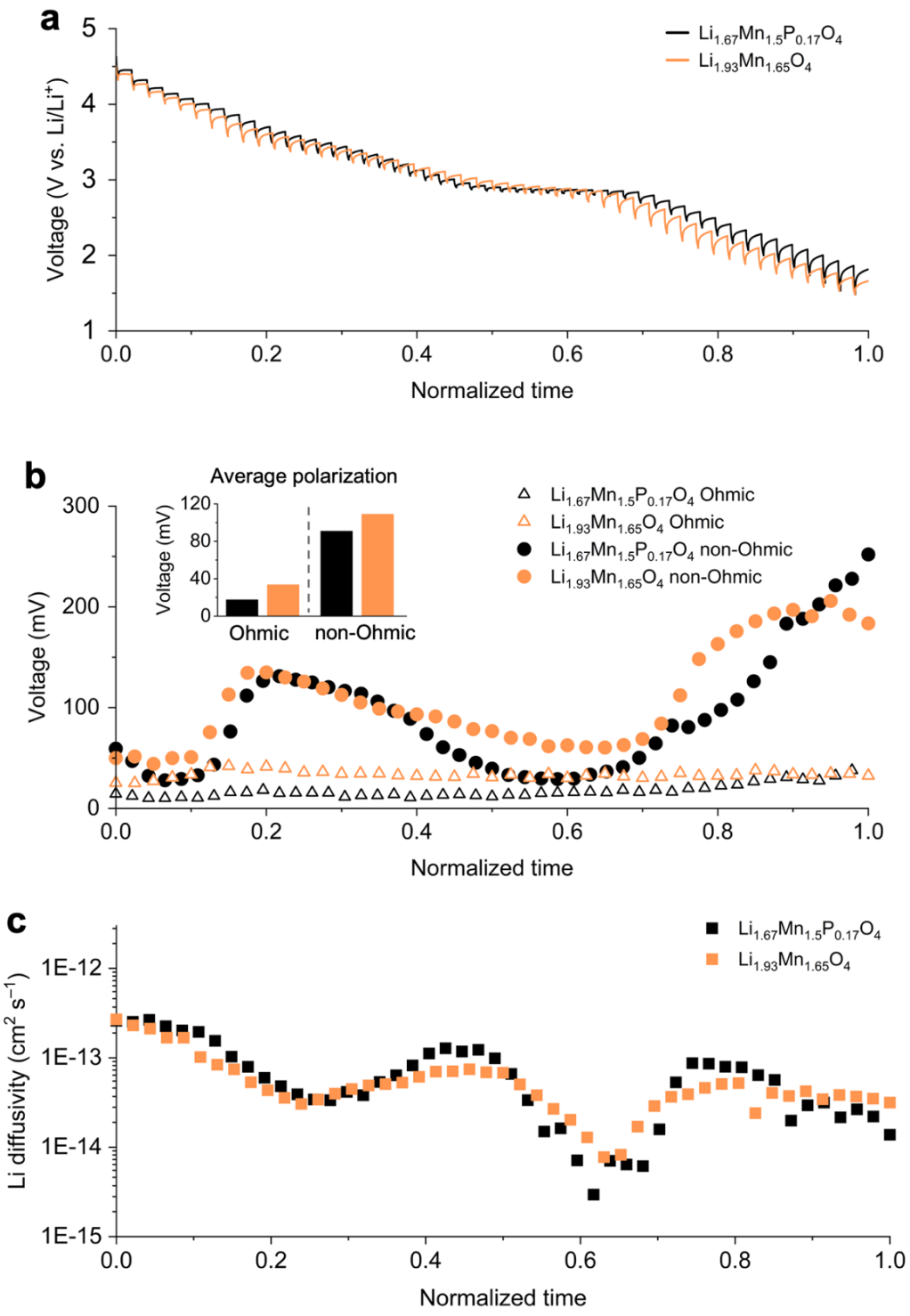

Supplementary Figure 10 | GITT measurement of $Li_{1.67}Mn_{1.5}P_{0.17}O_4$ and $Li_{1.93}Mn_{1.65}O_4$. a, GITT profiles in the first discharge cycle between 1.5 – 4.8 V vs Li/Li^+. A two-hour relaxation follows a 20 mA g^{-1} current pulse for 20 minutes in every charge/discharge step. **b,** Ohmic and non-Ohmic losses at each GITT step. **c,** Li^+ diffusivity values at each GITT step.

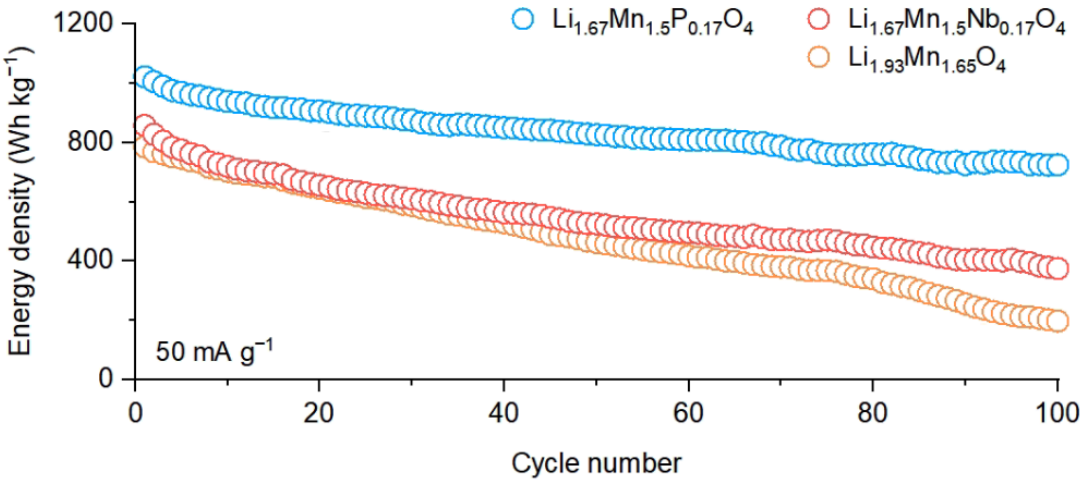

Supplementary Figure 11 | Discharge energy density retention of $Li_{1.67}Mn_{1.5}P_{0.17}O_4$, $Li_{1.67}Mn_{1.5}Nb_{0.17}O_4$ and $Li_{1.93}Mn_{1.65}O_4$ in 100 cycles between 1.5 – 4.8 V vs. Li/Li^+ at 50 mA g^{-1}, following the two initial formation cycles at 20 mA g^{-1} (not shown).

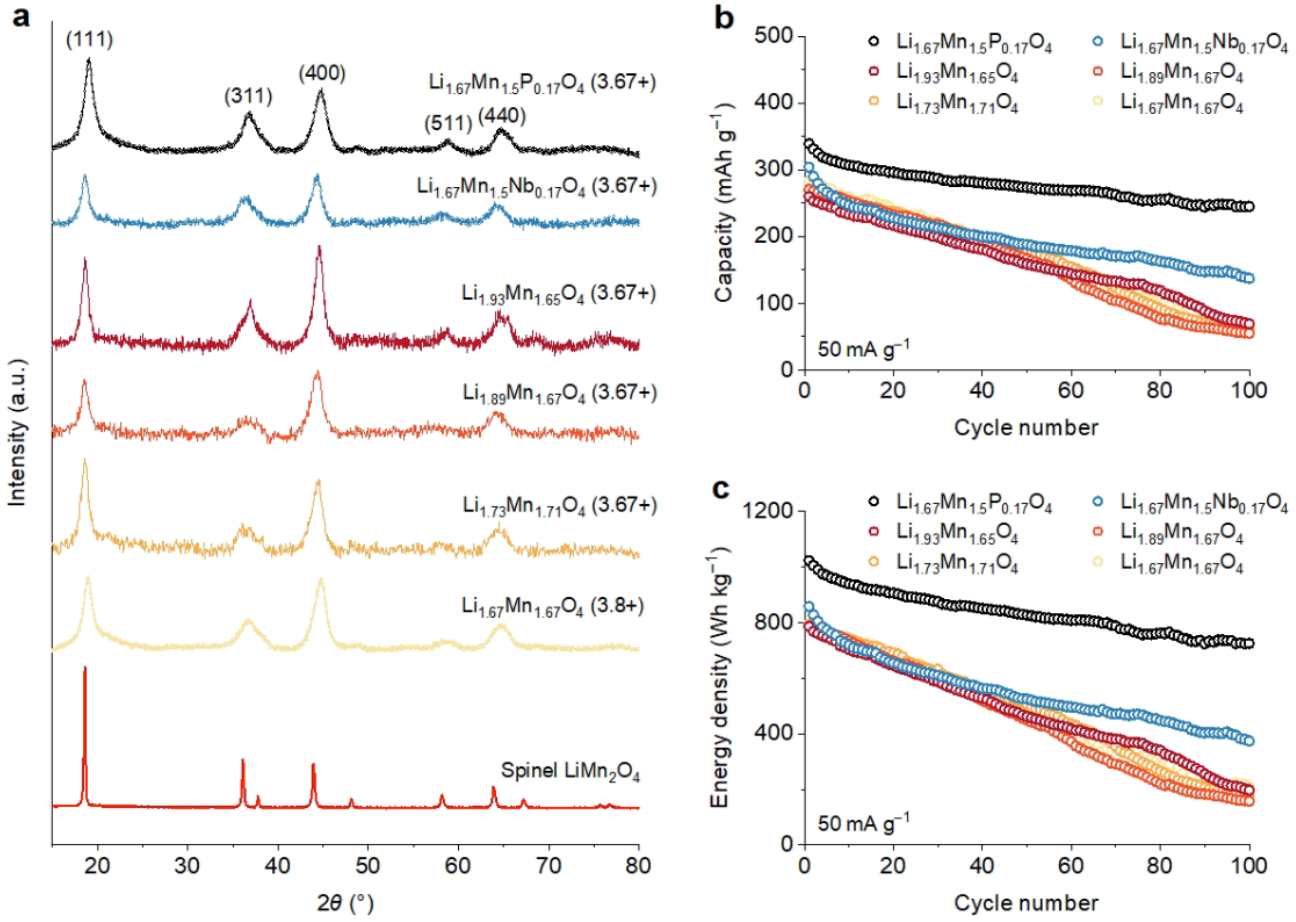

Supplementary Figure 12 | XRD patterns and cycling performance of different polyanion-free control groups. **a,** XRD patterns of $Li_{1.67}Mn_{1.5}P_{0.17}O_4$, different control groups, and reference spinel $LiMn_2O_4$. The number in the bracket indicates the initial Mn valence of the composition. **b,c,** Discharge capcity (b) and discharge energy density (c) retention of $Li_{1.67}Mn_{1.5}P_{0.17}O_4$ and different control groups in 100 cycles between 1.5 – 4.8 V vs. Li/Li^+ at 50 mA g^{-1}, following the two initial formation cycles at 20 mA g^{-1} (not shown).

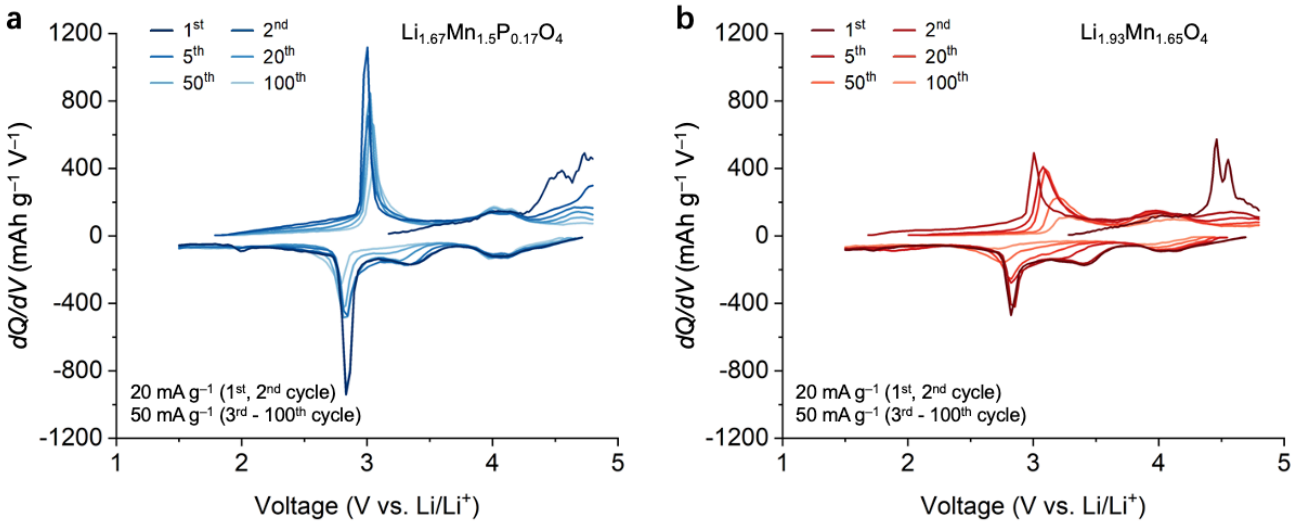

Supplementary Figure 13 | *dQ/dV* analysis for $Li_{1.67}Mn_{1.5}P_{0.17}O_4$ and $Li_{1.93}Mn_{1.65}O_4$. *dQ/dV* profiles for **a,** $Li_{1.67}Mn_{1.5}P_{0.17}O_4$ and **b,** $Li_{1.93}Mn_{1.65}O_4$, cycled between 1.5 – 4.8 V vs. Li/Li^+ at 20 mA g^{-1} in the initial two cycles, and at 50 mA g^{-1} in subsequent cycles.

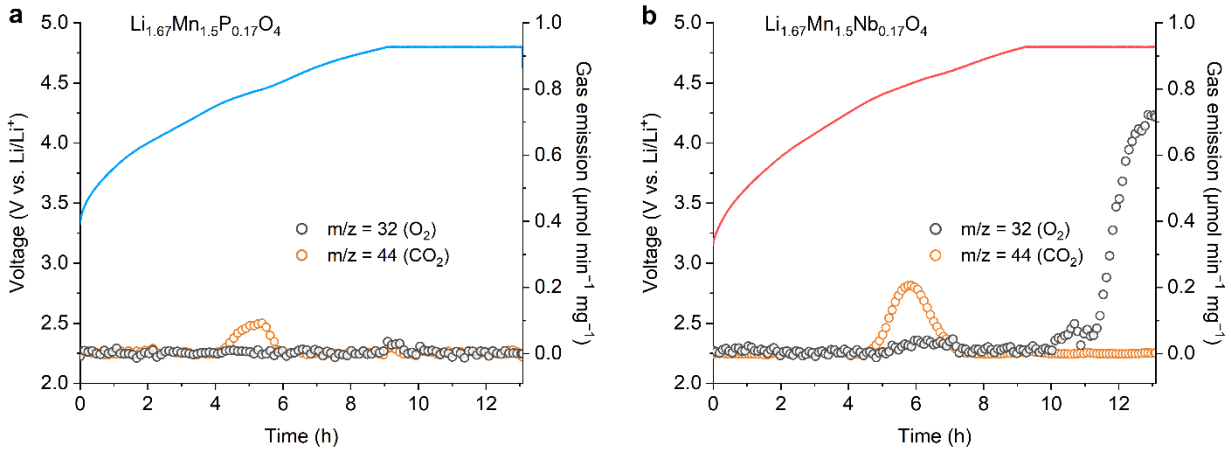

Supplementary Figure 14 | DEMS measurement in the first charge. CO_2 and O_2 evolution of **a,** $Li_{1.67}Mn_{1.5}P_{0.17}O_4$ and **b,** $Li_{1.67}Mn_{1.5}Nb_{0.17}O_4$, in the first charge to 4.8 V vs. Li/Li^+ at 15 mA g^{-1}, and held at 4.8 V for 4 h.

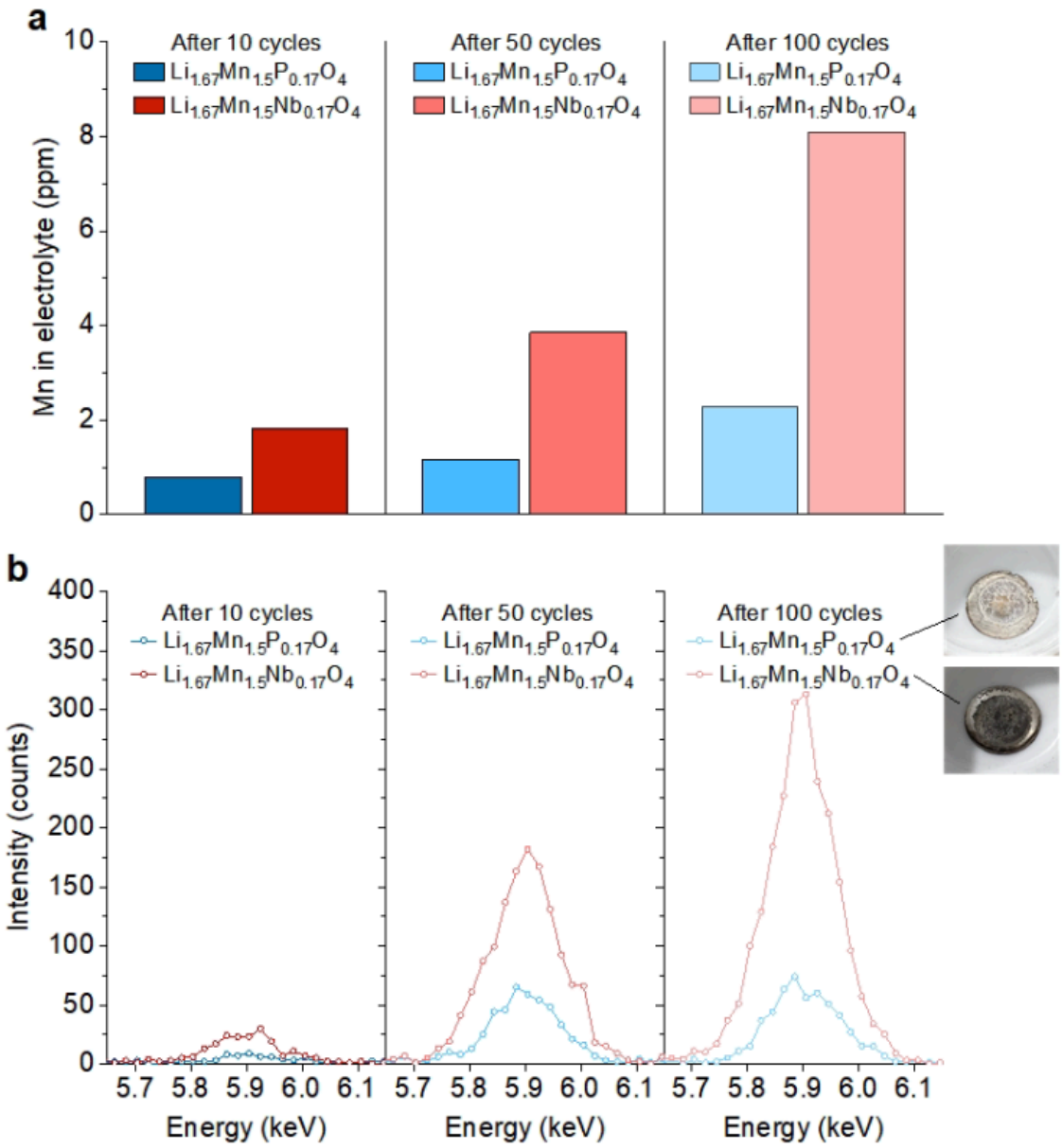

Supplementary Figure 15 | ICP-OES and XRF measurement of cycled $Li_{1.67}Mn_{1.5}P_{0.17}O_4$ and $Li_{1.67}Mn_{1.5}Nb_{0.17}O_4$ cells. a, ICP-OES measurement of dissolved Mn from cycled cathode film soaked in fresh electrolyte. **b,** XRF measurement of deposited Mn on the Li anode disc from cycled cells. The peak at 5.9 keV corresponds to the Mn Kα peak.

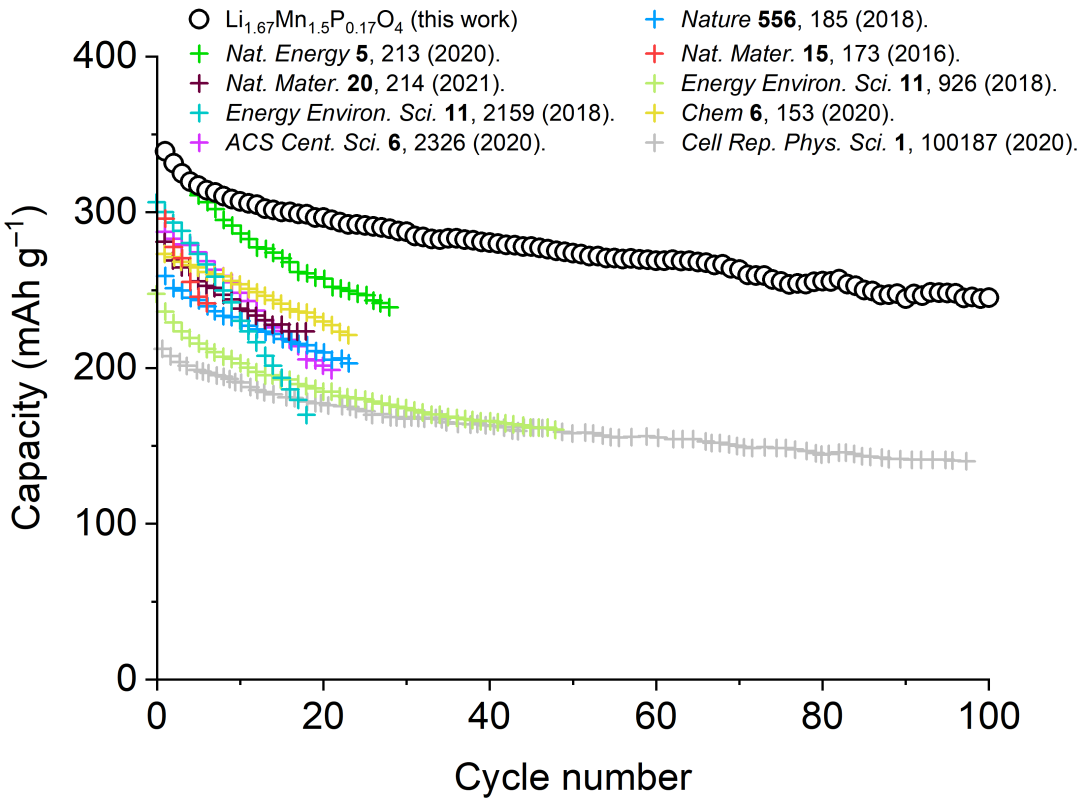

Supplementary Figure 16 | Cycling performance comparison of $Li_{1.67}Mn_{1.5}P_{0.17}O_4$ with DRX references in Supplementary Table 4.

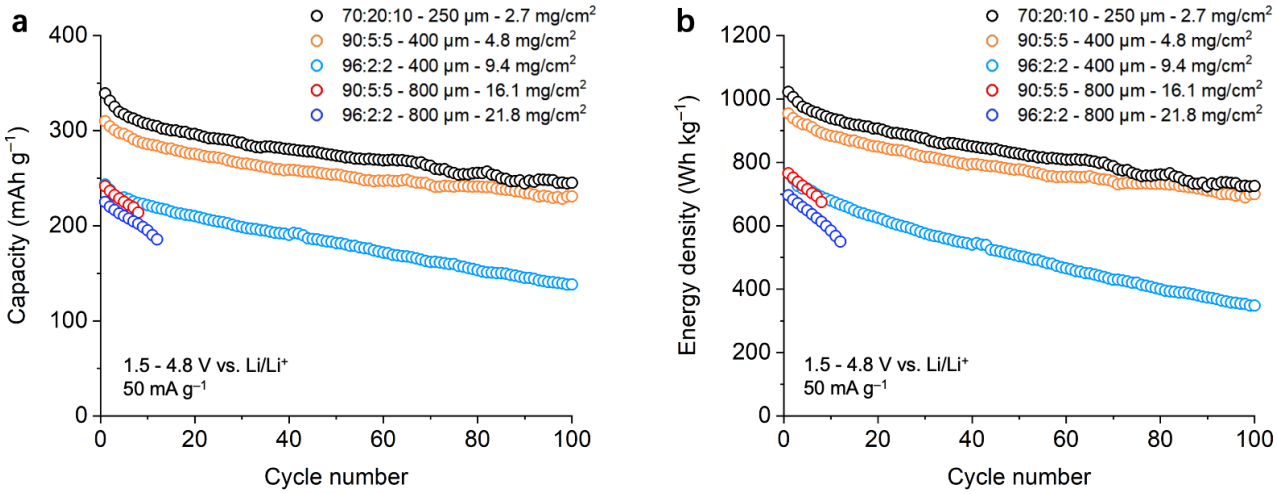

Supplementary Figure 17 | Cycling performance of $Li_{1.67}Mn_{1.5}P_{0.17}O_4$ with higher active material mass loading. **a,** Capacity retention. **b,** Discharge energy density retention. The cells were cycled between 1.5 – 4.8 V vs. Li/Li^+ at 50 mA g^{-1}, following two initial formation cycles at 20 mA g^{-1} (not shown). The legend reads: cathode active material:conductive carbon:PVDF binder weight ratio – doctor blade gap – electrode active material mass loading.

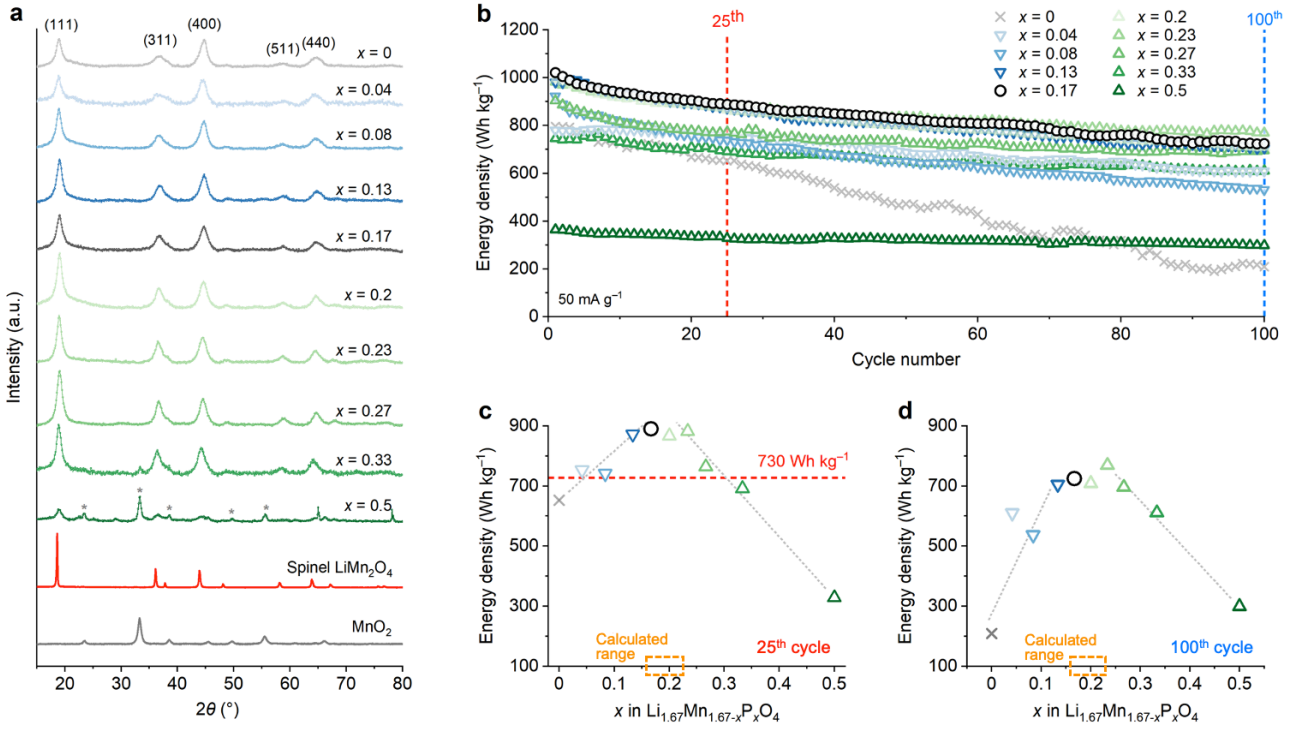

Supplementary Figure 18 | Structure and cycling of $Li_{1.67}Mn_{1.67-x}P_xO_4$ ($0 \leq x \leq 0.5$). a, XRD patterns. **b,** Discharge energy density in the first 100 cycles, between 1.5 – 4.8 V vs. Li/Li^+ at 50 mA g^{-1}, after two formation cycles at 20 mA g^{-1} (not shown). **c,** Discharge energy densities taken at the 25th cycle (counted after the two formation cycles). The red dashed line indicates the benchmark value for comparison. **d,** Discharge energy densities taken at the 100th cycle (counted after the two formation cycles). The orange dashed rectangle indicates the predicted optimal range of x calculated from design (Supplementary Note 1).

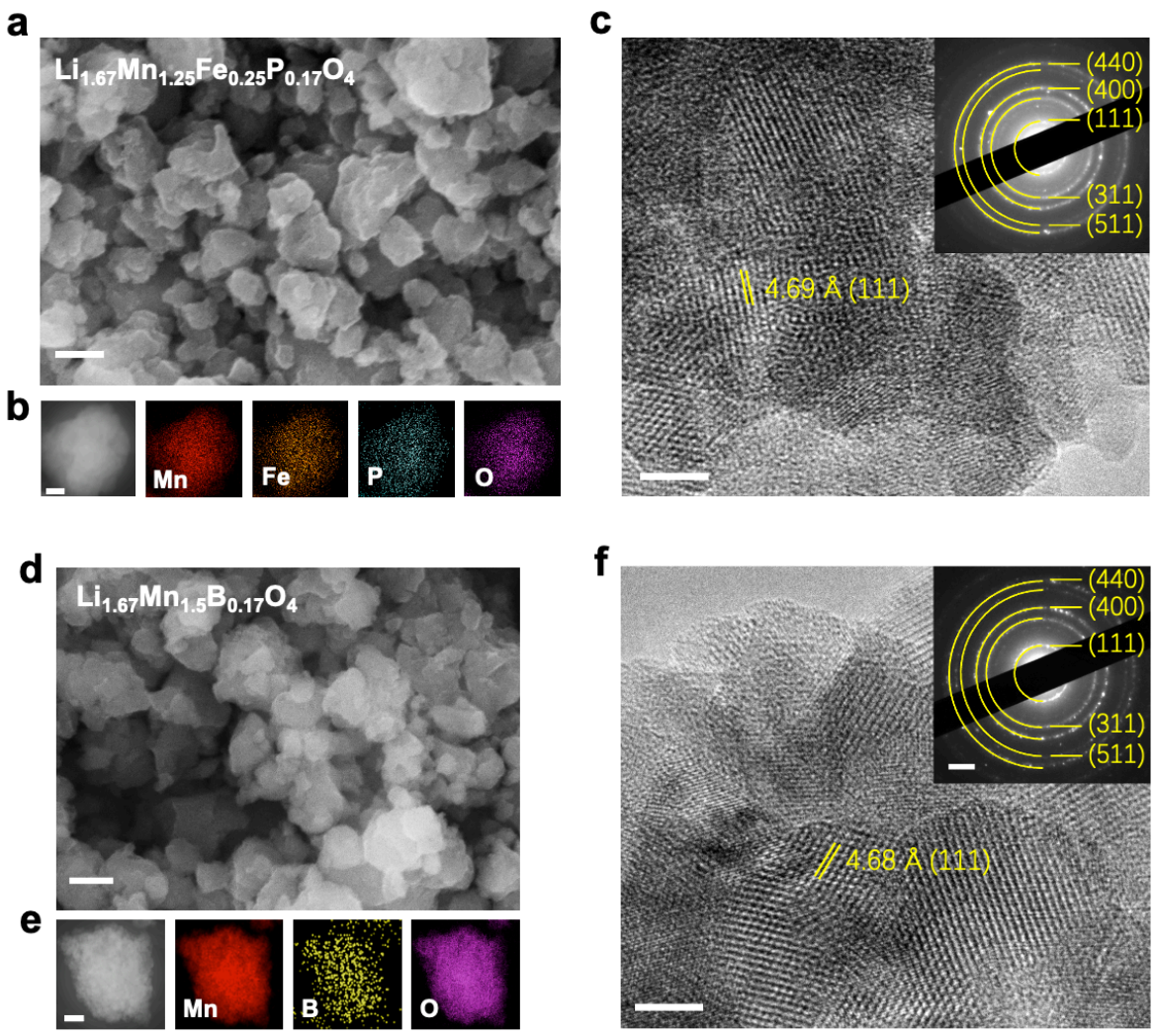

Supplementary Figure 19 | Morphology of $Li_{1.67}Mn_{1.25}Fe_{0.25}P_{0.17}O_4$. and $Li_{1.67}Mn_{1.5}B_{0.17}O_4$. a, SEM image of $Li_{1.67}Mn_{1.25}Fe_{0.25}P_{0.17}O_4$. Scale bar, 200 nm. **b,** STEM-EDS mapping of $Li_{1.67}Mn_{1.25}Fe_{0.25}P_{0.17}O_4$. Scale bar, 100 nm. **c,** TEM image of $Li_{1.67}Mn_{1.25}Fe_{0.25}P_{0.17}O_4$. Scale bar, 5 nm. Inset: SAED pattern. Scale bar, 2 nm^{-1}. **d,** SEM image of $Li_{1.67}Mn_{1.5}B_{0.17}O_4$. Scale bar, 200 nm. **e,** STEM-EDS mapping of $Li_{1.67}Mn_{1.5}B_{0.17}O_4$. Scale bar, 100 nm. **f,** TEM image of $Li_{1.67}Mn_{1.5}B_{0.17}O_4$. Scale bar, 5 nm. Inset: SAED pattern. Scale bar, 2 nm^{-1}.

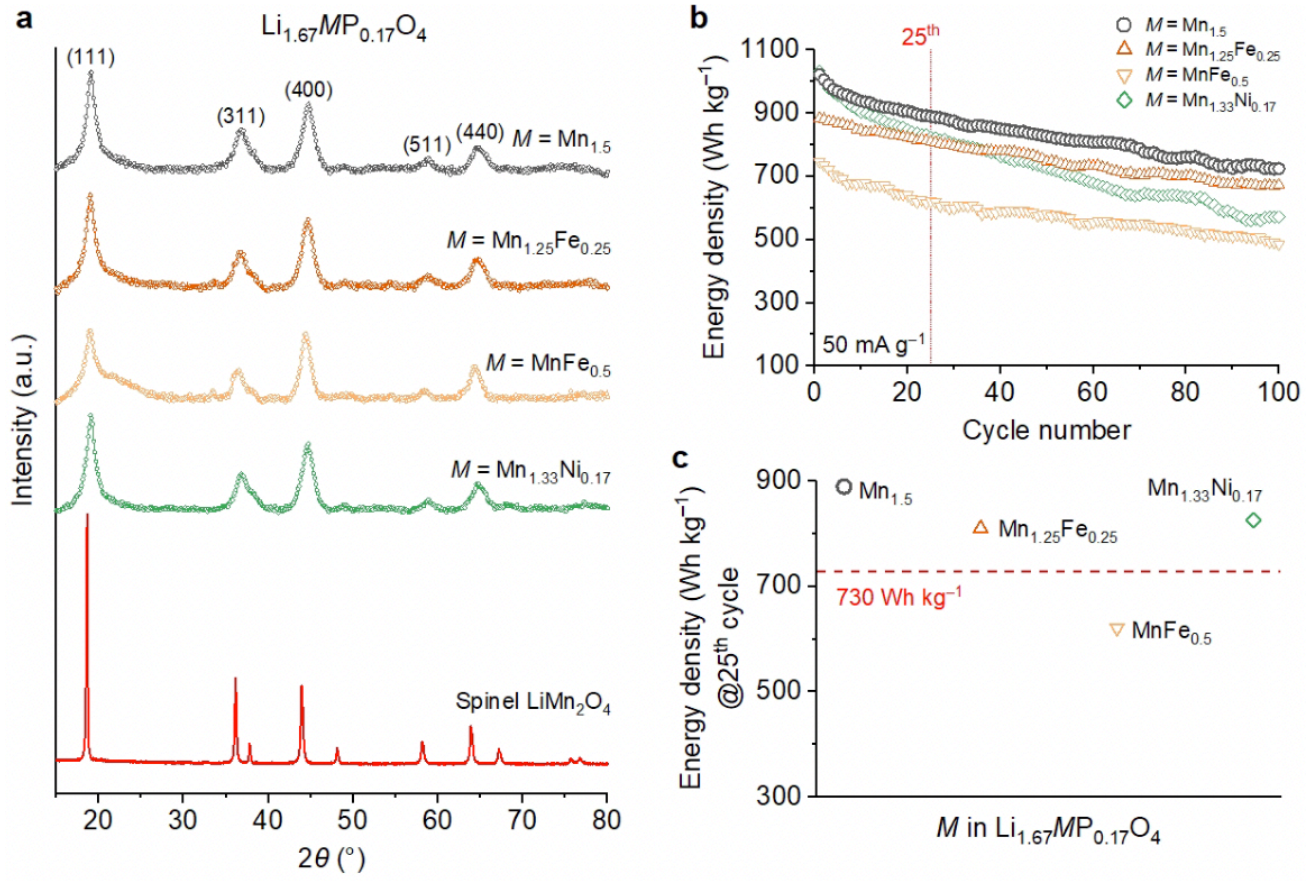

Supplementary Figure 20 | Structure and cycling of $Li_{1.67}MP_{0.17}O_4$. a, XRD patterns. **b,** Discharge energy density in the first 100 cycles, between 1.5 – 4.8 V vs. Li/Li^+ at 50 mA g^{-1}, after two formation cycles at 20 mA g^{-1} (not shown). **c,** Discharge energy densities taken at the 25th cycle (counted after the two formation cycles). The red dashed line indicates the benchmark value for comparison.

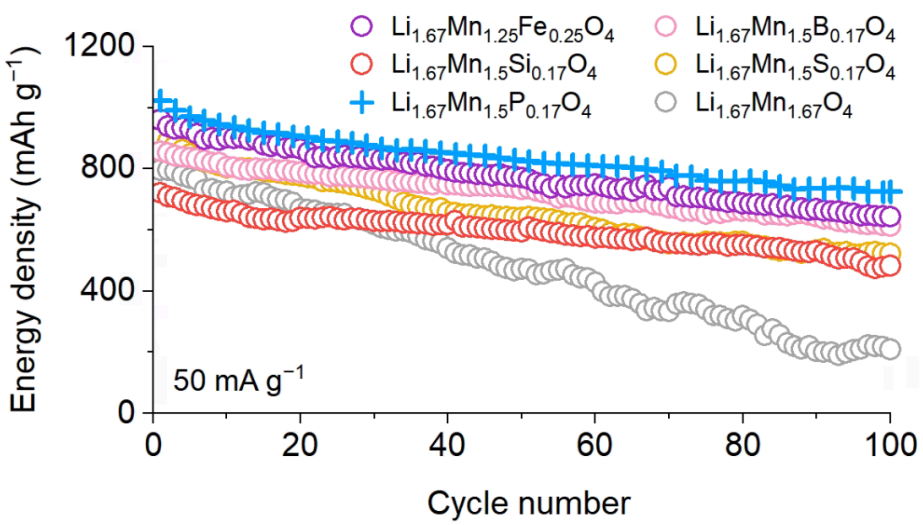

Supplementary Figure 21 | Discharge energy density of $Li_{1.67}Mn_{1.25}Fe_{0.25}P_{0.17}O_4$ and $Li_{1.67}Mn_{1.5}X_{0.17}O_4$ (X = B, Si, S) in the first 100 cycles, between 1.5 – 4.8 V vs. Li/Li^+ at 50 mA g^{-1}, after two formation cycles at 20 mA g^{-1} (not shown). Data for $Li_{1.67}Mn_{1.5}P_{0.17}O_4$ and $Li_{1.67}Mn_{1.67}O_4$ are also shown for reference.

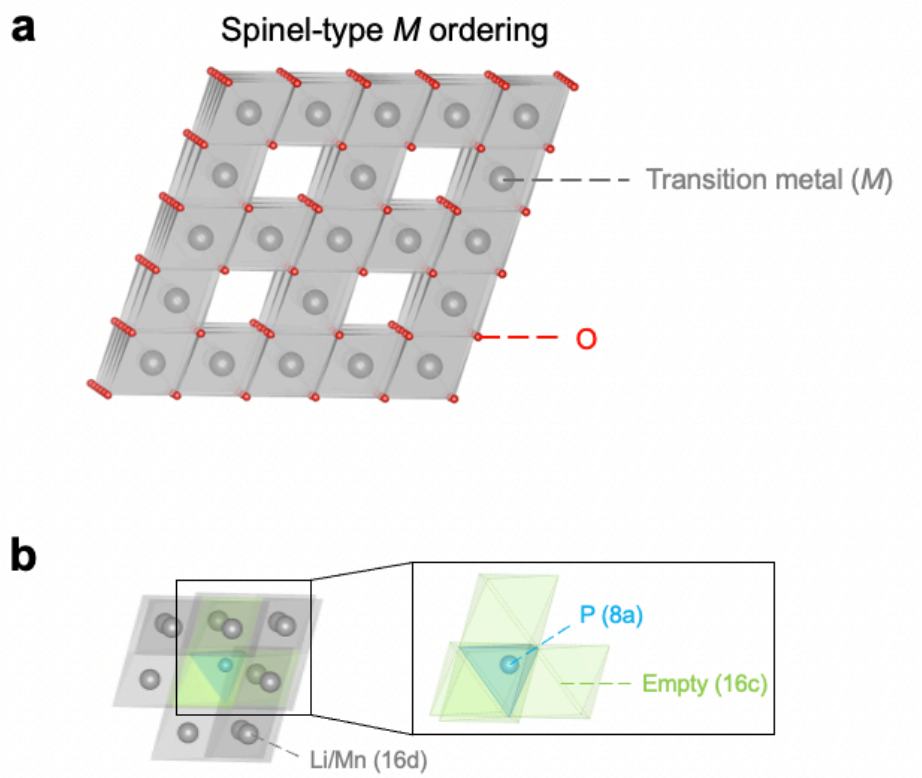

Supplementary Figure 22 | a, Spinel-type ordering of transition metal ions. **b,** Li/Mn occupied octahedra corner-shared with a polyanion tetrahedron, and empty octahedra face-shared with a polyanion tetrahedron.

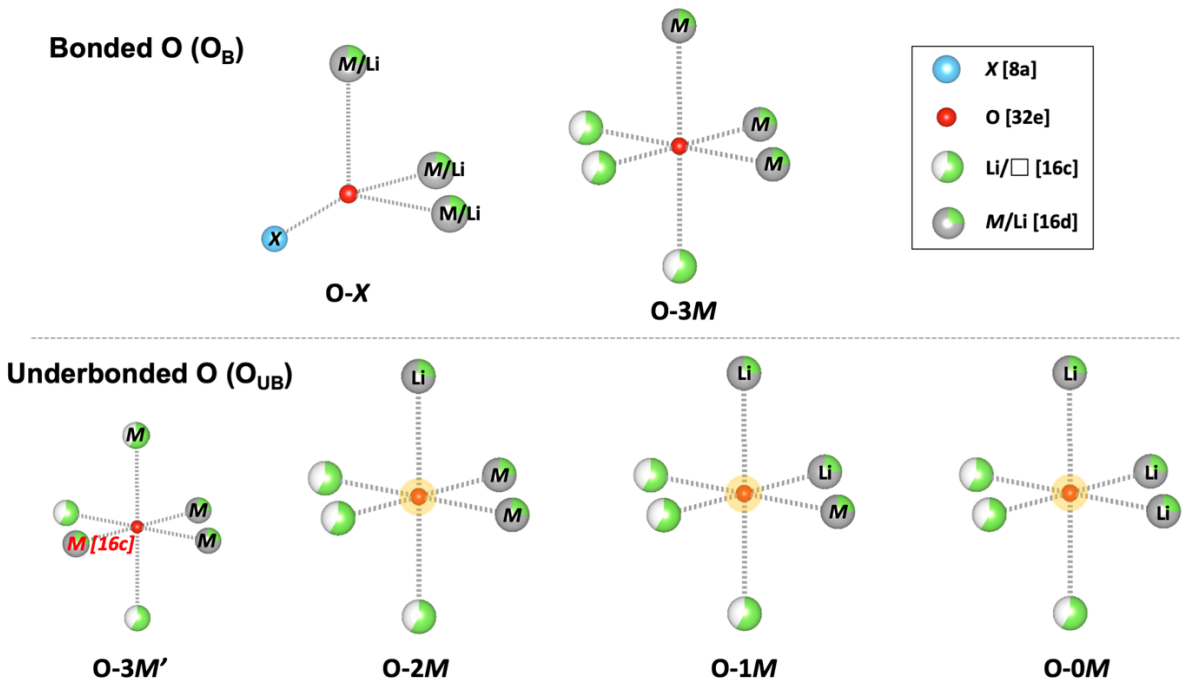

Supplementary Figure 23 | Different oxygen local environments. Bonded oxide ions (O-*X* and O-3*M*) and underbonded oxide ions (O-3*M*', O-2*M*, O-1*M* and O-0*M*).

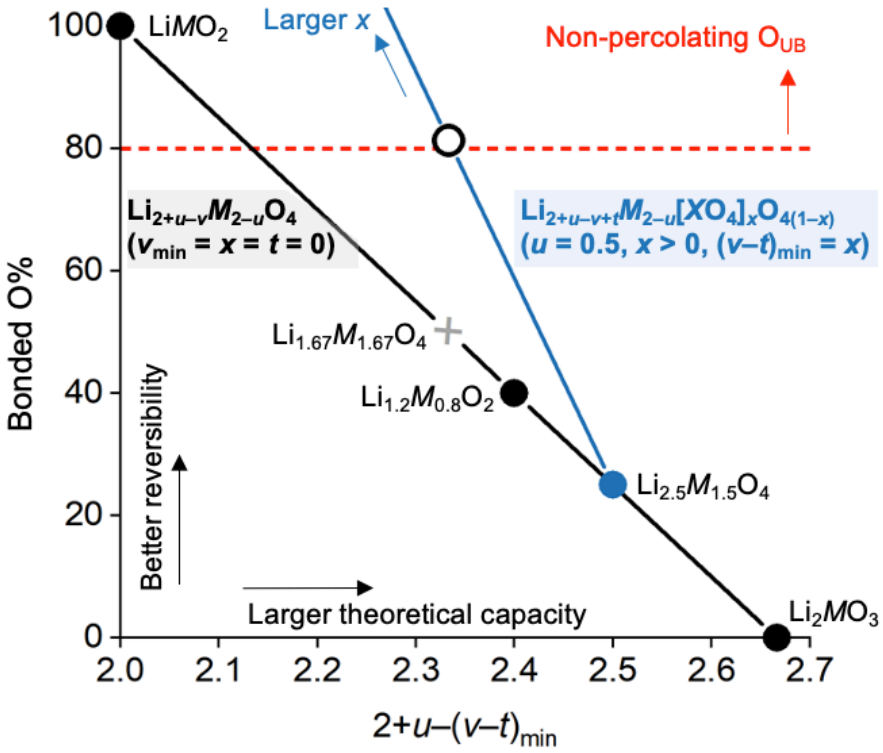

Supplementary Figure 24 | Bonded O (O_B) ratio in stoichiometries with different theoretical lithiation limits $2+u-(v-t)_{min}$. The black line represents polyanion-free compositions, and the blue line represents polyanionic compositions (with $u = 0.5$). The red dashed line marks the percolation threshold for underbonded O, above which (< 20 at% O_{UB}) compositions are considered to have good cycling stability.

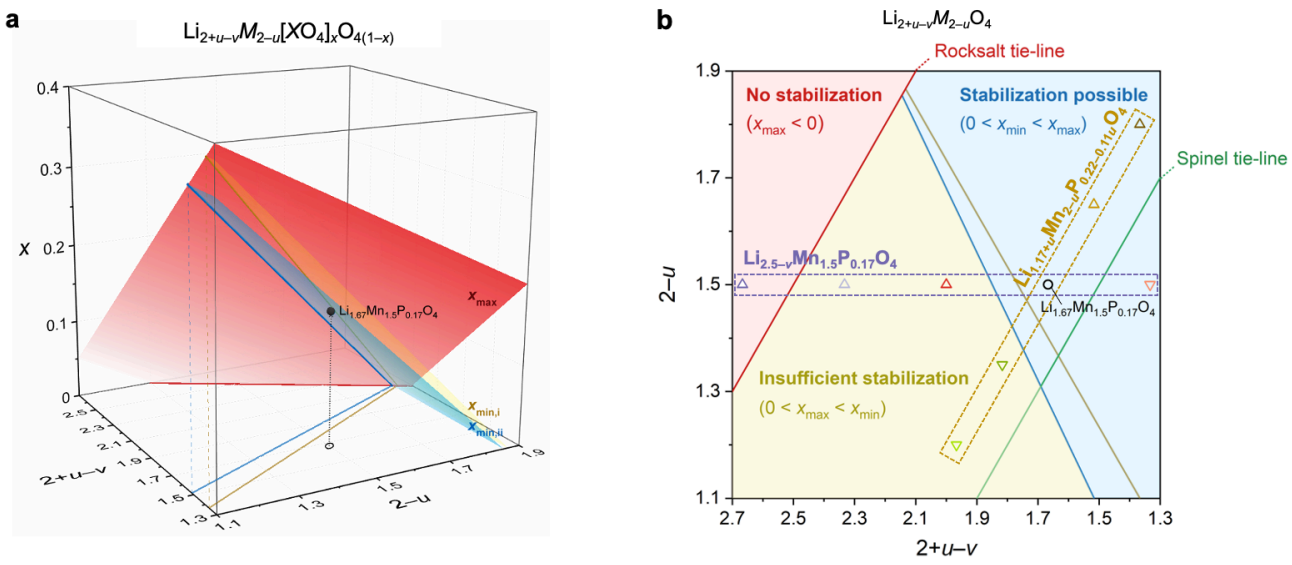

Supplementary Figure 25 | Range of polyanion content, *x*, in $Li_{2+u-v}M_{2-u}[XO_4]_xO_{4(1-x)}$. a, x_{max} and x_{min} under different Li and *M* content. **b,** Projection of plot in (**a**) onto the x-y plane, showing different regimes of polyanion stabilization for different base compositions $Li_{2+u-v}M_{2-u}O_4$. Base compositions of $Li_{2.5-v}Mn_{1.5}P_{0.17}O_4$ ($v = -0.17$, 0.17, 0.5, 0.83, 1.17) and $Li_{1.17+u}Mn_{2-u}P_{0.22-0.11u}O_4$ (u = 0.2, 0.35, 0.5, 0.65, 0.8), studied in Supplementary Note 3, are marked.

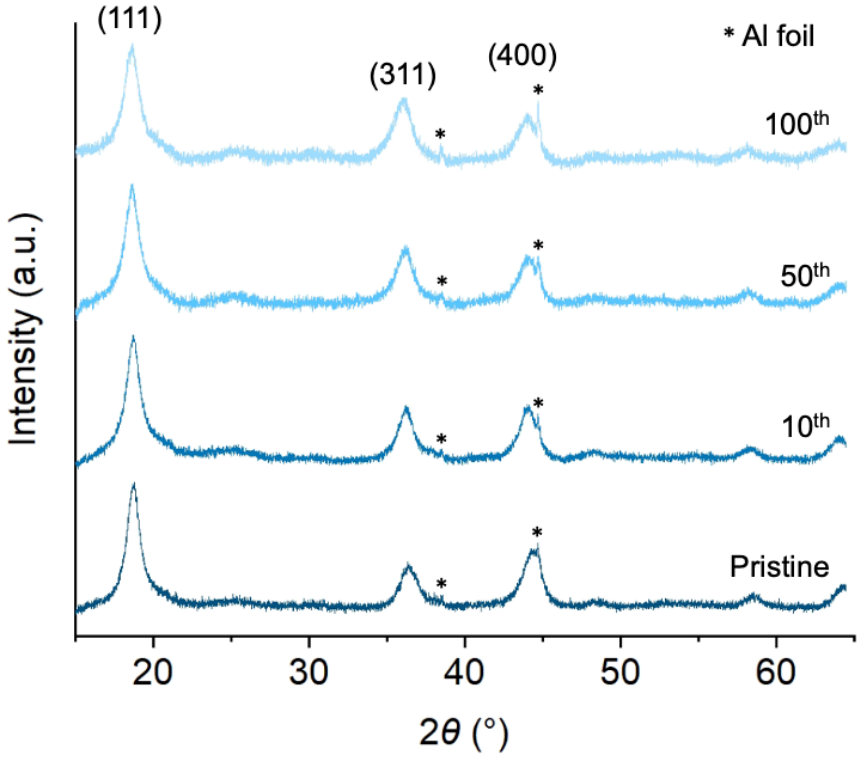

Supplementary Figure 26 | Ex situ XRD of pristine $Li_{1.67}Mn_{1.5}P_{0.17}O_4$ cathode and after 10, 50 and 100 cycles.

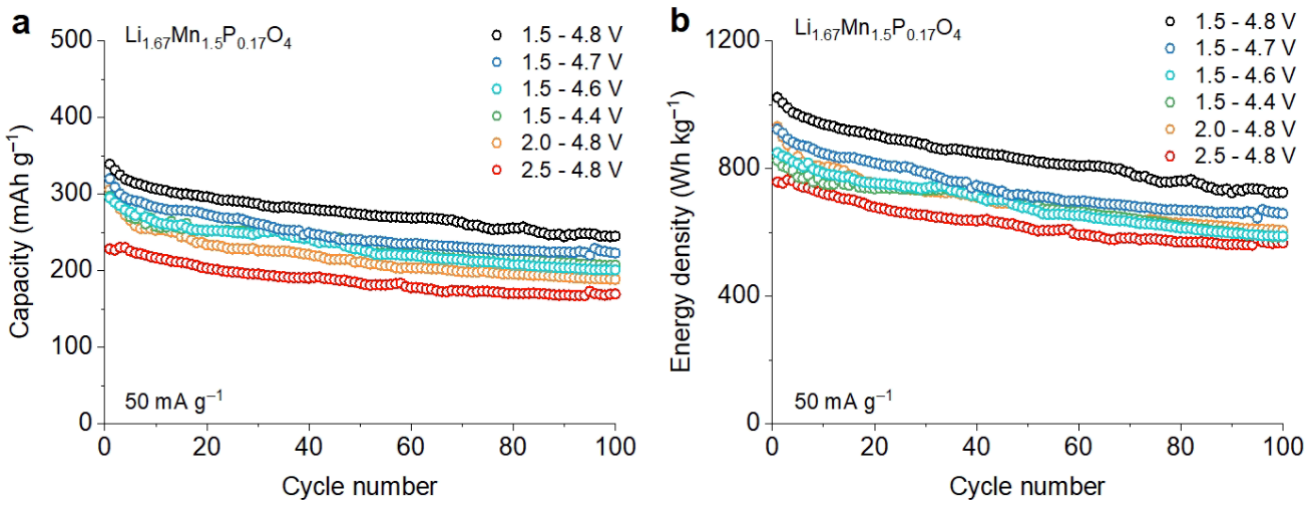

Supplementary Figure 27 | Cycling performance of $Li_{1.67}Mn_{1.5}P_{0.17}O_4$ under different voltage windows. a,b, Discharge capacity (a) and discharge energy density (b) retention of $Li_{1.67}Mn_{1.5}P_{0.17}O_4$ in 100 cycles between different voltage windows (vs. Li/Li^+) at 50 mA g^{-1}, following the two initial formation cycles at 20 mA g^{-1} (not shown).

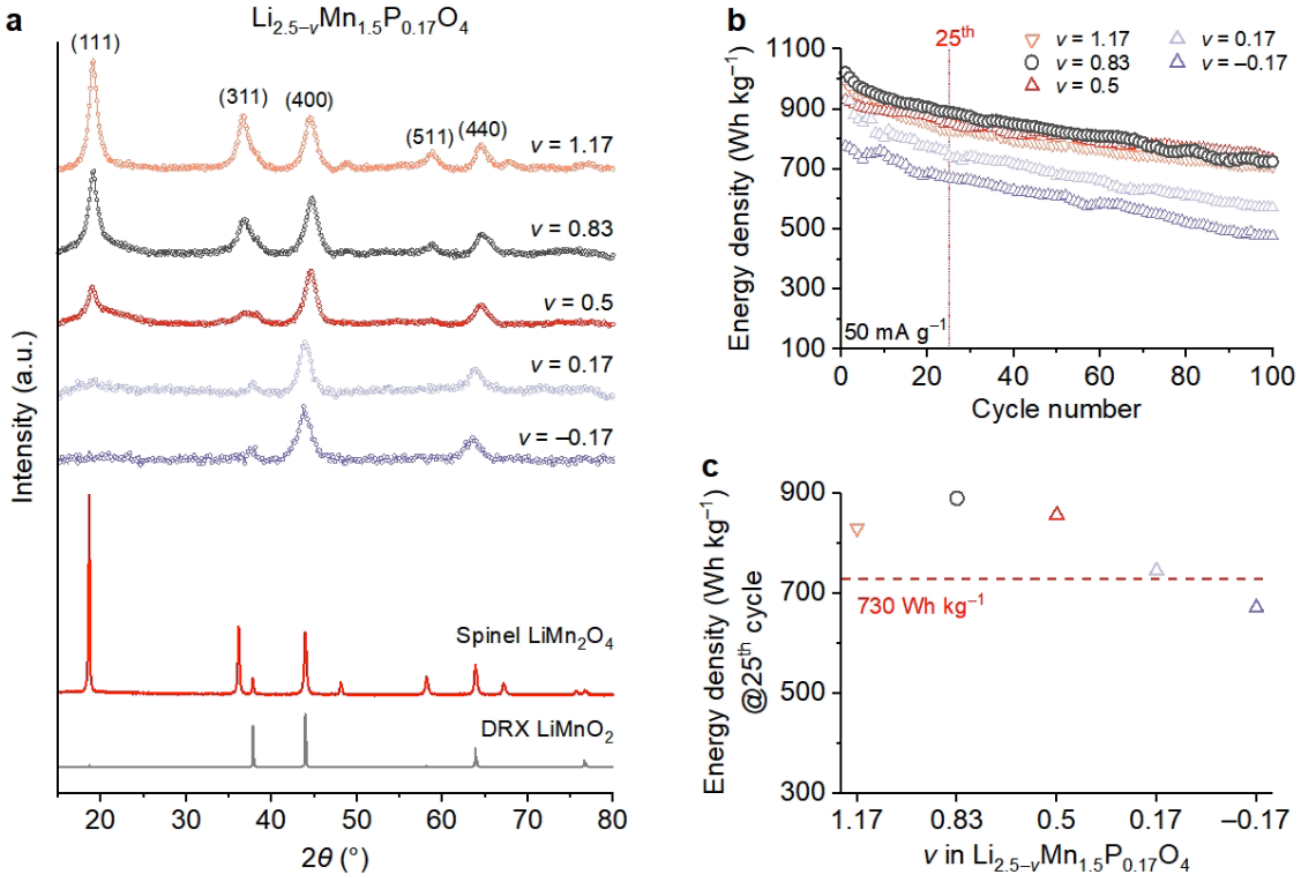

Supplementary Figure 28 | Structure and cycling of $Li_{2.5-v}Mn_{1.5}P_{0.17}O_4$ (v = –0.17, 0.17, 0.5, 0.83, 1.17). a, XRD patterns. Note that the XRD pattern for DRX $LiMnO_2$ is calculated from the configuration of a completely random distribution of Li and Mn in 16c and 16d octahedral sites. **b,** Discharge energy density in the first 100 cycles, between 1.5 – 4.8 V vs. Li/Li^+ at 50 mA g^{-1}, after two formation cycles at 20 mA g^{-1} (not shown). **c,** Discharge energy densities taken at the 25th cycle (counted after the two formation cycles). The red dashed line indicates the benchmark value for comparison.

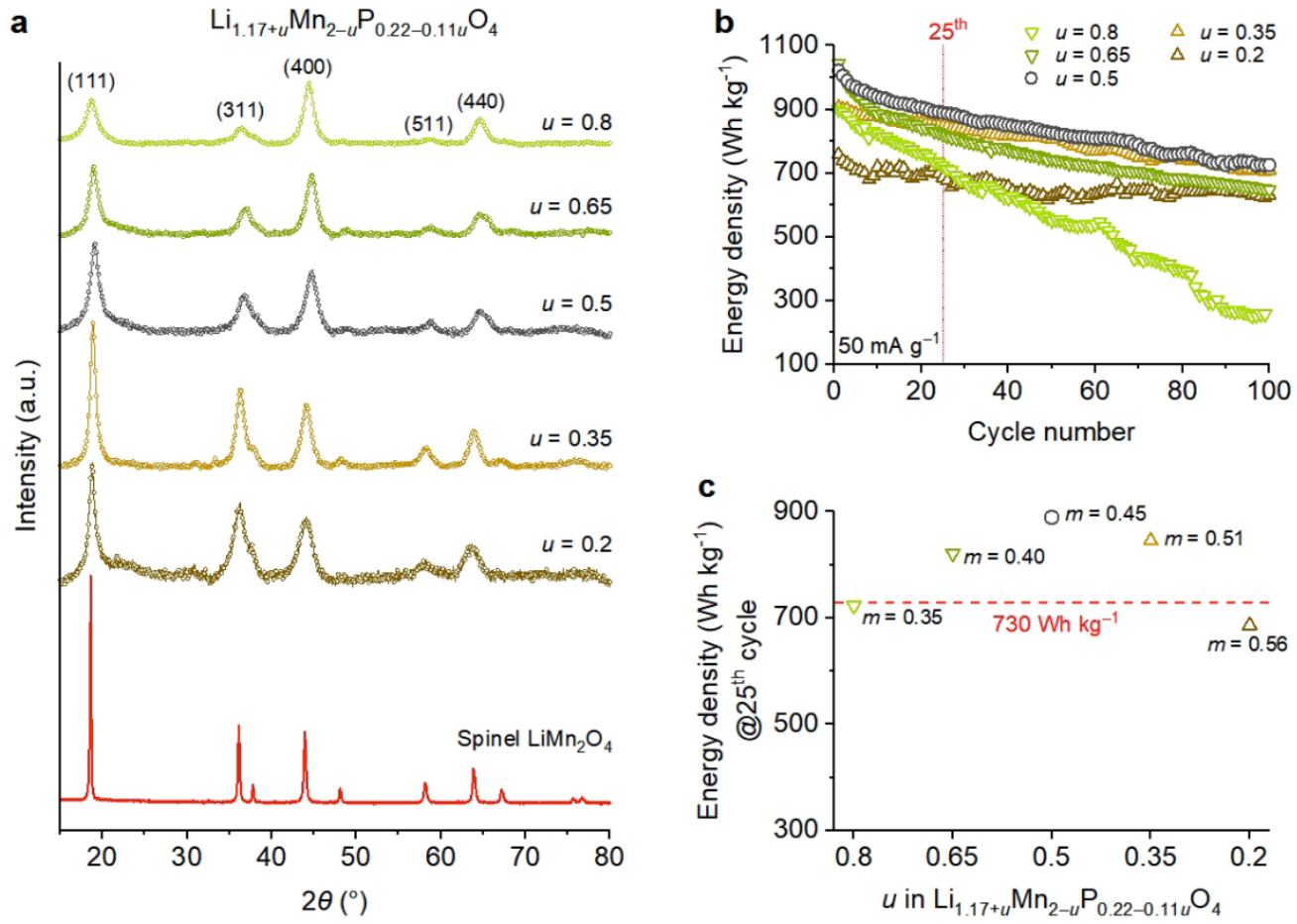

Supplementary Figure 29 | Structure and cycling of $Li_{1.17+u}Mn_{2-u}P_{0.22-0.11u}O_4$ (u = 0.2, 0.35, 0.5, 0.65, 0.8). a, XRD patterns. **b,** Discharge energy density in the first 100 cycles, between 1.5 – 4.8 V vs. Li/Li^+ at 50 mA g^{-1}, after two formation cycles at 20 mA g^{-1} (not shown). **c,** Discharge energy densities taken at the 25th cycle (counted after the two formation cycles). The red dashed line indicates the benchmark value for comparison. The effective M/O ratio, $m_e = (2-u)/(3.12+0.44u)$, is calculated and labeled.

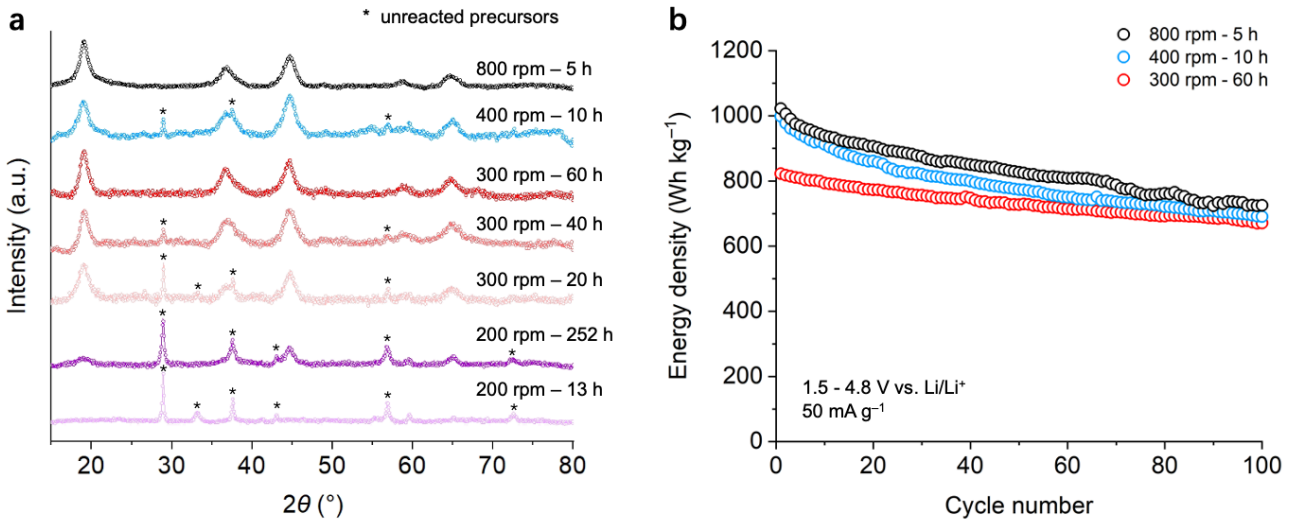

Supplementary Figure 30 | Comparison of $Li_{1.67}Mn_{1.5}P_{0.17}O_4$ synthesized under different ball milling conditions. a, XRD patterns of $Li_{1.67}Mn_{1.5}P_{0.17}O_4$ synthesized at 200, 300, 400, and 800 rpm, under different milling durations. **b,** Discharge energy density retention of $Li_{1.67}Mn_{1.5}P_{0.17}O_4$ synthesized at 300, 400, and 800 rpm, cycled between 1.5 – 4.8 V vs. Li/Li^+ and at 50 mA g^{-1} (following two initial formation cycles at 20 mA g^{-1}).

Supplementary Table 1 | Elemental molar ratios of selected compositions measured by ICP-MS.

Target cation composition	Measured cation composition
$Li_{1.667}Mn_{1.500}P_{0.167}$	$Li_{1.667}Mn_{1.478}P_{0.184}$
$Li_{1.667}Mn_{1.500}B_{0.167}$	$Li_{1.667}Mn_{1.424}B_{0.130}$
$Li_{1.667}Mn_{1.250}Fe_{0.250}P_{0.167}$	$Li_{1.667}Mn_{1.196}Fe_{0.248}P_{0.187}$

Supplementary Table 2 | Structural parameters of $Li_{1.67}Mn_{1.5}P_{0.17}O_4$ from X-ray diffraction Rietveld refinement.

$Li_{1.67}Mn_{1.5}P_{0.17}O_4$	Element	Site	*x*	*y*	*z*	Occupancy	U_{iso}
Space group: $Fd\bar{3}m$	Li	8a	0.125	0.125	0.125	0.25(3)	0.024(1)
a = 8.1527(5) Å	P	8a	0.125	0.125	0.125	0.17(3)	0.024(1)
R_p = 5.39%	Li	16c	0	0	0	0.46(1)	0.084(2)
R_{wp} = 6.55%	Mn	16c	0	0	0	0.05(1)	0.084(2)
χ^2 = 1.41	Li	16d	0.25	0.5	0.25	0.25(3)	0.010(1)
*	Mn	16d	0.25	0.5	0.25	0.70(3)	0.010(1)
	O	32e	0.2616(7)	0.2616(7)	0.2616(7)	0.9965(3)	0.024(1)

* The structure shown in Figure 2g (cubic $Fd\bar{3}m$, space group 227) is used as the input model. Initial atomic positions were allocated based on the stoichiometry $Li_{1.67}Mn_{1.5}P_{0.17}O_4$. P atoms were intially evenly distributed in 8a sites, while Mn were allocated to 16d sites, with the total molar amount fixed. We tried distributing Mn in 8a sites and P in 16d sites, but resulted in poor R factors. During refinement, we allow Mn in 16c and P in 8b sites, as well as variable occupancy ratio and coordinates of O. Li atoms were allocated last according to the starting model, since they have negligible affect on the refinement result. The final best-fit model indicates minor Mn in 16c sites and a 0.75% deficiency in O. No additional impurities were found in the diffraction pattern.

Supplementary Table 3 | Structural parameters of $Li_{1.67}Mn_{1.5}P_{0.17}O_4$ from neutron powder diffraction Rietveld refinement.

$Li_{1.67}Mn_{1.5}P_{0.17}O_4$	Element	Site	*x*	*y*	*z*	Occupancy	U_{iso}
Space group: $Fd\bar{3}m$	Li	8a	0.125	0.125	0.125	0.25	0.37(2)
a = 8.1188(1) Å	P	8a	0.125	0.125	0.125	0.17	0.37(2)
R_p = 5.163%	Li	16c	0	0	0	0.46	0.036(3)
*	Mn	16c	0	0	0	0.05	0.036(3)
	Li	16d	0.25	0.5	0.25	0.25	0.004(1)
	Mn	16d	0.25	0.5	0.25	0.70	0.004(1)
	O	32e	0.2625	0.2625	0.2625	0.993	0.009(1)

* The output from XRD refinement in Supplementary Table 2 is used as the input model. Li is allowed to allocate freely among 8a, 16c, and 16d sites.

Supplementary Table 4 | Comparison of DRXPS with DRX and other common cathodes reported in the literature.

Structure	Composition	Energy density (Wh kg^{-1})*	Capacity retention (cycles**)	(Co+Ni) /*M* ratio	Voltage range (V vs. Li/Li^+)	Current density (mA g^{-1})	Ref
DRXPS	$Li_{1.67}Mn_{1.5}P_{0.17}O_4$	1122	72% (100)	0	1.5 – 4.8	50	This work
DRX	$Li_4Mn_2O_5$	953	81% (6)	0	1.2 – 4.8	20	5
DRX	$Li_2Mn_{2/3}Nb_{1/3}O_2F$	849	78% (23)	0	1.5 – 4.8	20	6
DRX	$Li_{1.9}Mn_{1.95}O_{2.05}F_{0.95}$	960	68% (48)	0	2.0 – 4.8	22	7
DRX	$Li_{1.171}Mn_{0.343}V_{0.486}O_{1.8}F_{0.2}$	862	56% (18)	0	1.5 – 4.8	20	8
DRX	$Li_{1.2}Mn_{0.6}Nb_{0.2}O_2$	650	66% (98)	0	1.5 – 4.8	100	9
DRX	$Li_{7/6}Mn_{2/3}P_{1/6}O_2$	890	69% (21)	0	1.5 – 4.8	10	10
DRX	$Li_{1.25}Mn_{0.75}O_{1.33}F_{0.67}$	822	81% (23)	0	1.5 – 5.0	20	11
DRX	$Li_{1.3}Mn_{0.2}Co_{0.1}Cr_{0.1}Ti_{0.1}Nb_{0.2}O_{1.7}F_{0.3}$	955	79% (18)	0.14	1.5 – 4.7	20	12
DRX-spinel	$Li_{1.68}Mn_{1.6}O_{3.7}F_{0.3}$	1103	72% (28)	0	1.5 – 4.8	50	13
Spinel	$LiMn_2O_4$	490	60% (98)	0	3.0 – 4.3	130	14
Spinel	$LiNi_{0.5}Mn_{1.5}O_4$	590	98% (98)	0.25	3.5 – 5.0	118	15
Layered	$LiCoO_2$	720	95% (98)	1	3.0 – 4.45	90	16
Layered	$LiNi_{1/3}Co_{1/3}Mn_{1/3}O_2$	610	98% (98)	0.67	2.8 – 4.3	100	17
Layered	$LiNi_{0.8}Co_{0.1}Mn_{0.1}O_2$	780	81% (98)	0.9	2.8 – 4.3	100	17
Layered	$LiNi_{0.8}Co_{0.15}Al_{0.05}O_2$	760	90% (98)	0.95	2.8 – 4.3	175	18
Layered	$Li_{1.2}Ni_{0.13}Co_{0.13}Mn_{0.54}O_2$	900	68% (98)	0.33	2.0 – 4.8	50	19
Olivine	$LiFePO_4$	510	97% (98)	0	2.5 – 4.1	30	20
Olivine	$LiMn_{0.8}Fe_{0.2}PO_4$	650	91% (98)	0	2.7 – 4.25	30	21

* Refers to the discharge energy density in the first cycle.

** Counted from the 3rd cycle (initial two cycles are considered as formation cycles. E.g., '100' means 100 cycles after the two formation cycles).

Supplementary Table 5 | Volumetric energy density calculations of DRXPS and common cathode materials.

Material	Theoretical density ($g\ cm^{-3}$)[a]	Electrode density ($g\ cm^{-3}$)[b]	Grav. energy density ($Wh\ kg^{-1}$, material)[c]	Vol. energy density ($Wh\ L^{-1}$, material)[d]	Vol. energy density ($Wh\ L^{-1}$, electrode)[e]
$Li_{1.67}Mn_{1.5}P_{0.17}O_4$	4.00	2.8	1122	4488	2200
$LiCoO_2$	5.12	3.9	720	3686	2900 (@4.45V)
$LiMn_2O_4$	4.04	3.2	490	1980	1300
$LiFePO_4$	3.68	2.3	510	1877	1240

[a] Calculated by (weight of atoms in unit cell)/(unit cell volume).

[b] Electrode density of $Li_{1.67}Mn_{1.5}P_{0.17}O_4$ was calculated by (weight of electrode)/(electrode area × electrode thickness), and the electrode thickness was measured by a micrometer (does not include current collector). Data for $LiCoO_2$, $LiMn_2O_4$ and $LiFePO_4$ were taken from Table 1 in Supplementary Reference 22.

[c] Taken in the initial discharge cycle.

[d] Calculated by (grav. energy density) × (theoretical density).

[e] Vol. energy density of $Li_{1.67}Mn_{1.5}P_{0.17}O_4$ was calculated by (grav. energy density) × (electrode density) × (weight ratio of active material in the electrode). Other data were taken from Table 1 in Supplementary Reference 22.

Supplementary references

1. Bontchev, R. P. et al. $Co_5BP_3O_{14}$: The first borophosphate with planar BO_3 groups connected to PO_4 tetrahedra. *Inorg. Chem.* **35**, 6910-6911 (1996).
2. Huang, Y. M. et al. Lithium manganese spinel cathodes for lithium-ion batteries. *Adv. Energy Mater.* **11**, 2000997 (2021).
3. Lorenz, C. D. & Ziff, R. M. Universality of the excess number of clusters and the crossing probability function in three-dimensional percolation. *J. Phys.: a-Math. Gen.* **31**, 8147-8157 (1998).
4. Urban, A., Lee, J. & Ceder, G. The configurational space of rocksalt-type oxides for high-capacity lithium battery electrodes. *Adv. Energy Mater.* **4**, 1400478 (2014).
5. Freire, M. et al. A new active Li-Mn-O compound for high energy density Li-ion batteries. *Nat. Mater.* **15**, 173 (2016).
6. Lee, J. et al. Reversible Mn^{2+}/Mn^{4+} double redox in lithium-excess cathode materials. *Nature* **556**, 185 (2018).
7. House, R. A. et al. Design principles for high transition metal capacity in dirordered rocksalt Li-ion cathodes. *Energy Environ. Sci.* **11**, 926 (2018).
8. Kitchaev, D. A. *et al.* Design principles for high transition metal capacity in disordered rocksalt Li-ion cathodes. *Energ Environ. Sci.* **11**, 2159 (2018).
9. Kwon, D. H. et al. The impact of surface structure transformations on the performance of Li-excess cation-disordered rocksalt cathodes. *Cell Rep. Phys. Sci.* **1**, 100187 (2020).
10. Sawamura, M. et al. Nanostructured $LiMnO_2$ with Li_3PO_4 integrated at the atomic scale for high-energy electrode materials with reversible anionic redox. *ACS Central Sci.* **6**, 2326-2338 (2020).
11. Lun, Z. Y. et al. Design Principles for High-Capacity Mn-Based Cation-Disordered Rocksalt Cathodes. *Chem* **6**, 153 (2020).
12. Lun, Z. Y. et al. Cation-disordered rocksalt-type high-entropy cathodes for Li-ion batteries. *Nat. Mater.* **20**, 214 (2021).
13. Ji, H. W. et al. Ultrahigh power and energy density in partially ordered lithium-ion cathode materials. *Nat. Energy* **5**, 213-221 (2020).
14. Lee, M. J., Lee, S., Oh, P., Kim, Y. & Cho, J. High Performance $LiMn_2O_4$ cathode materials grown with epitaxial layered nanostructure for Li-ion batteries. *Nano Lett.* **14**, 993-999 (2014).
15. Zhou, L., Zhao, D. Y. & Lou, X. W. $LiNi_{0.5}Mn_{1.5}O_4$ hollow structures as high-performance cathodes for lithium-ion batteries. *Angew. Chem. Int. Edit.* **51**, 239-241 (2012).
16. Xu, N. et al. A facile strategy to improve the cycle stability of 4.45 V $LiCoO_2$ cathode in gel electrolyte system via succinonitrile additive under elevated temperature. *Solid State Ionics* **341**, 115049 (2019).
17. Noh, H. J., Youn, S., Yoon, C. S. & Sun, Y. K. Comparison of the structural and electrochemical properties of layered $Li[Ni_xCo_yMn_z]O_2$ (x=1/3, 0.5, 0.6, 0.7, 0.8 and 0.85) cathode material for lithium-ion batteries. *J. Power Sources* **233**, 121-130 (2013).
18. Xie, H. B., Du, K., Hu, G. R., Peng, Z. D. & Cao, Y. B. The role of sodium in $LiNi_{0.8}Co_{0.15}Al_{0.05}O_2$ cathode material and its electrochemical behaviors. *J. Phys. Chem.* C. **120**, 3235-3241 (2016).
19. Ku, L. et al. Enhanced electrochemical performances of layered-spinel heterostructured lithium-rich $Li_{1.2}Ni_{0.13}Co_{0.13}Mn_{0.54}O_2$ cathode materials. *Chem. Eng. J.* **370**, 499-507 (2019).
20. Huang, H., Yin, S. C. & Nazar, L. F. Approaching theoretical capacity of $LiFePO_4$ at room temperature at high rates. *Electrochem. Solid St.* **4**, A170-A172 (2001).
21. Martha, S. K. et al. $LiMn_{0.8}Fe_{0.2}PO_4$: An advanced cathode material for rechargeable lithium batteries. *Angew. Chem. Int. Edit.* **48**, 8559-8563 (2009).
22. Zheng, J. M. et al. Li- and Mn-rich cathode materials: challenges to commercialization. *Adv. Energy Mater.* **7**, 1601284 (2017).

Lithium-ion batteries

https://doi.org/10.1038/s41560-024-01664-x

Polyanions stabilize anion redox

Jagjit Nanda

Traditionally, lithium-ion battery cathodes face a trade-off between the energy density afforded by high-voltage anion reduction–oxidation and long-term stability. Now, incorporating polyanion motifs into a disordered oxide crystal structure is shown to stabilize the oxygen sublattice, improving capacity retention at high energy densities.

It is critical but challenging to develop lithium-ion battery electrodes that simultaneously address energy density, stability, and cost issues[1,2]. For example, high-energy-density positive electrodes (cathodes) such as disordered rock salts or lithium- and manganese (Mn)-rich layered oxides offer extra capacity beyond the conventional cation redox rection in oxide cathodes, enabled through lithium-rich chemistry and the associated anion redox mechanism; however, they suffer from low stability and energy efficiency[3–5]. One reason for the poor stability is that anion redox triggers structural rearrangements, which can lead to the loss of lattice oxygen as gaseous oxygen. In contrast, cathodes such as lithium iron phosphate ($LiFePO_4$) have much higher stability because of the structural rigidity of the polyanions (PO_4^{3-}) but exhibit lower energy density with no known anion-based capacity[6].

Now, writing in *Nature Energy*[7], Ju Li, Yanhao Dong and colleagues explain that the instability of anion redox in cathodes is related to the presence of underbonded (labile) oxygen ions. These ions form a percolative pathway in the lattice, as shown in Fig. 1a. When these labile oxygens are electrochemically oxidized, they can diffuse to the particle surface, leading to loss of lattice oxygen and thereby destabilizing the structure. Li, Dong and colleagues propose a cathode design that incorporates polyanion units (XO_4) with strongly covalent X–O bonds into the parent oxide lattice. This incorporation disrupts the percolation of underbonded oxygen (Fig. 1b), thereby mitigating oxygen loss and producing high energy density from mixed cation and anion redox reactions.

Practically speaking, producing a hybrid structure of polyanionic oxide cathodes is extremely challenging. In most lithium-ion oxide cathodes, the oxygen anions are arranged in a cubic close-packed array, with all octahedral interstices filled by cations, either randomly (as in disordered rock salts) or segregated into alternating lithium and transition-metal layers (as in layered oxides). There is a fundamental incompatibility between the polyanion units and this oxide framework structure. The polyanion XO_4 tetrahedra unit requires the face-sharing octahedra sites to be vacant, and there are no octahedral vacancies in disordered rock salts or layered oxides. Additionally, the typical covalent X–O bond length is shorter than what the larger tetrahedral interstices in the oxide structures can accommodate.

In their work, using only low-cost elements, Li, Dong and colleagues successfully integrate polyanion motifs into oxide-based cathodes, producing a crystal structure designated disordered rocksalt–polyanionic spinel (DRXPS). They show a family of DRXPS with the general formula $Li_{2+u-v}M_{2-u}[XO_4]_xO_{4(1-x)}$, where M is a transition metal (Mn, Fe), and four types of XO_4 polyanion are demonstrated (PO_4, BO_4, SiO_4 and SO_4). The compositions achieved include $Li_{1.67}Mn_{1.5}P_{0.17}O_4$, $Li_{1.67}Mn_{1.5}B_{0.17}O_4$ and $Li_{1.67}Mn_{1.25}Fe_{0.25}P_{0.17}O_4$, among others.

The research team tackle the incompatibility obstacle between polyanion and oxide structures through a judicious design of composition and the use of mechanochemical synthesis. The design favours the formation of a spinel-style arrangement of atoms, while the mechanochemical synthesis permits structural disordering. Spinel has the same oxygen anion framework as in disordered rock salts or layered oxides, but with a distinct filling pattern for the interstitial sites: a lower cation-to-oxygen ratio (3:4 compared to 1:1), with only half of the octahedral interstices filled.

Li, Dong and colleagues selected manganese as the dominant transition metal, which is known to favour spinel-type ordering, as seen in the compound $LiMn_2O_4$ (ref. 8). They further adjusted the values of u, v and x so that the overall composition becomes closer to the 3:4 occupancy rule of an ideal spinel (with the polyanion-forming

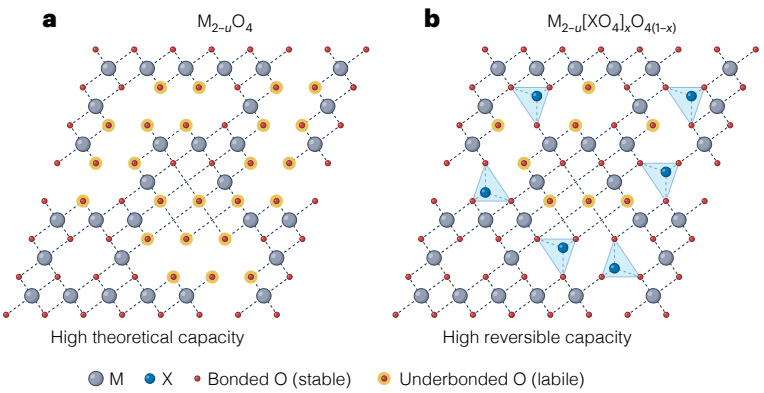

Fig. 1 | Design of disordered rocksalt–polyanionic spinel cathodes. **a**, The structure of a representative conventional anion redox cathode in the delithiated state. The percolative pathway for underbonded oxygen leads to oxygen loss and the instability of oxygen redox. **b**, Incorporating polyanion units disrupts the pathway for oxygen diffusion, which in turn stabilizes the oxygen sublattice and improves the stability of anion redox. Reproduced from ref. 7, Springer Nature.

element X treated as a cation in this crystallographic consideration). In the spinel-type lattice, XO_4 polyanions can be stabilized within the ordered arrangement of vacant octahedral sites. By mechanochemical synthesis, the larger-than-conventional polyanion size is kinetically stabilized. In contrast, using conventional high-temperature calcination synthesis would probably result in phase separation before the formation of such a metastable and locally distorted DRXPS structure.

Compared to the polyanion-free counterparts, Li, Dong and colleagues report improved cycling stability for the DRXPS cathodes. This improvement is mainly attributed to the increased reversibility of anion redox, thanks to the mechanism by which polyanions stabilize the oxygen lattice against the release of oxygen gas, as discussed earlier. Better rate performance and higher lithium diffusivity than conventional disordered rock salts are also observed, probably related to the fast three-dimensional lithium diffusion channels present in the spinel-based crystal structure. In half-cells, promising performance is reported, with gravimetric energy densities exceeding 1,100 Watt-hours per kilogram and over 70% retention after 100 cycles.

Overall, the research team have reported a promising class of lithium-ion cathodes that provides opportunities for more detailed investigation and follow-up work. While energy-intensive ball-milling may help to achieve the desired cathode composition, it does not provide control over particle morphology and size. Therefore, it is worth exploring alternative synthesis methods beyond the reported mechanochemical method. The performance reported so far has been on half-cells, and challenges may arise in demonstrating high capacity and stability in full cells with graphite anodes. The relationship between polyanion incorporation and the detailed anion redox mechanism remains unclear. At present, the hypothesis regarding how polyanions suppress oxygen release requires further in-depth study. Additionally, the surface reactivity with the electrolyte and the subsequent surface reconstruction warrants further investigation.

Jagjit Nanda[1,2] ✉
[1]SLAC-Stanford Battery Center, SLAC National Accelerator Laboratory, Menlo Park, CA, USA. [2]Department of Materials Science and Engineering, Stanford University, Stanford, CA, USA.
✉e-mail: jnanda@slac.stanford.edu

Published online: 15 November 2024

References

1. Goodenough, J. B. & Kim, Y. *Chem. Mater.* **22**, 587–603 (2010).
2. Manthiram, A. *Nat. Commun.* **11**, 1550 (2020).
3. Clément, R. J., Lun, Z. & Ceder, G. *Energy Environ. Sci.* **13**, 345–373 (2020).
4. Csernica, P. M. et al. *Nat. Energy* **6**, 642–652 (2021).
5. House, R. A. et al. *Nat. Energy* **6**, 781–789 (2021).
6. Masquelier, C. & Croguennec, L. *Chem. Rev.* **113**, 6552–6591 (2013).
7. Huang, Y. et al. *Nat. Energy* https://doi.org/10.1038/S41560-024-01615-6 (2024).
8. Huang, Y. et al. *Adv. Energy Mater.* **11**, 2000997 (2021).

Competing interests

The author declares no competing interests.